nature energy

Supplementary information

https://doi.org/10.1038/s41560-024-01689-2

Self-assembled bilayer for perovskite solar cells with improved tolerance against thermal stresses

In the format provided by the authors and unedited

Table of Content:

Supplementary Figure 1. Schematic diagram of SAB structure and formation 4
Supplementary Figure 2. X-ray photoelectron spectroscopy full spectra of 2PACz, TATPA, and SAB 5
Supplementary Figure 3. Characterizations of SAB before and after annealing 6
Supplementary Figure 4. Attenuated Total-reflective Fourier Transform Infrared Spectroscopy spectra of 2PACz film 7
Supplementary Figure 5. Reaction mechanism of H^+ catalyzed methoxylation of TATPA with CD_3OD 8
Supplementary Figure 6. ^{1}H-NMR spectra of the reacted mixture of TATPA and CD_3OD 9
Supplementary Figure 7. ToF-SIMS results of SAB 10
Supplementary Figure 8. Characterization of the cross-linked SAB 11
Supplementary Figure 9. ^{1}H NMR spectrum of 2PACz 12
Supplementary Figure 10. ^{1}H NMR spectrum of NECz 13
Supplementary Figure 11. ^{1}H NMR spectrum of TATPA 14
Supplementary Figure 12. ^{1}H NMR Spectrum of NECz:TATPA:2PACz equals to 100:10:1 15
Supplementary Figure 13. Design rationale of DTBA-2PACz 17
Supplementary Figure 14. High-Resolution Mass Spectroscopy (HRMS) spectra of DTBA-2PACz 18
Supplementary Figure 15. ^{1}H-NMR spectra of as-reacted DTBA-2PACz 19
Supplementary Figure 16. C-H Heteronuclear single quantum coherence (HSQC) spectra of DTBA-2PACz 20
Supplementary Figure 17. ^{1}H-^{1}H correlation spectroscopy (COSY) NMR spectra of DTBA-2PACz 21
Supplementary Figure 18. Chemical structure of bisTATPA and SAB formation mechanism between 2PACz and bisTATPA 22
Supplementary Figure 19. ATR-FTIR spectra of bisTATPA and 2PACz based SAB before and after thermal annealing 23
Supplementary Figure 20. Formation mechanism of SABs based on 4PACz and PATPA 25
Supplementary Figure 21. ATR-FTIR spectra of TATPA-based SABs before and after thermal annealing 26
Supplementary Figure 22. HRMS spectra of the coupled product between DTBA and 4PACz 27
Supplementary Figure 23. HRMS spectra of the coupled product between DTBA and PATPA 28
Supplementary Figure 24. Structural characterization of 2PACz SAM 30

Supplementary Figure 25. Structural characterization of 2PACz SAM at increased precursor concentration 31
Supplementary Figure 26. GIWAXS results for SAM, SAB, and SAB with a concentrated 2PACz bottom layer 32
Supplementary Figure 27. Structural characterization of SAB 34
Supplementary Figure 28. KPFM surface potential images 35
Supplementary Figure 29. Contact potential difference (CPD) distribution of SAM, SAB before annealing and SAB after annealing 35
Supplementary Figure 30. Electrochemical approach measured molecular coverage 37
Supplementary Figure 31. EDS analysis showing the residues of SAM or SAB on the perovskite side of the buried interface 38
Supplementary Figure 32. Surface SEM photographs of perovskites 39
Supplementary Figure 33. GIWAXS integration of perovskite deposited on SAM and SAB 40
Supplementary Figure 34. Time-Resolved Photoluminescence characterization results of perovskite on SAM and SAB 42
Supplementary Figure 35. Photoluminescence characterization results of perovskite on SAM and SAB 43
Supplementary Figure 36. Transmission line model measurement on contact resistance of perovskite on SAM and SAB 44
Supplementary Figure 37. UPS characterization results of SAM and SAB 45
Supplementary Figure 38. A photograph and illustrative sketch of the double-cantilever beam (DCB) fabricated to measure the interface toughness G_C 46
Supplementary Figure 39. Adhesion energy measurements of the perovskite/HSC contact using and FTO as substrate 47
Supplementary Figure 40. Calculated adsorption energy between SAB and perovskite with different dihedral angle 48
Supplementary Figure 41. Statistic results for inverted PSCs with pristine 2PACz SAM and SAB hole-selective contact 49
Supplementary Figure 42. Independent measurement results from Shanghai Institute of Microsystem and information Technology, Chinese Academy of Sciences 52-53
Supplementary Figure 43. Photovoltaic parameters statistical distribution of PSCs using 4PACz and 4PACz:TATPA (SAB-4PACz) as hole-selective contacts 54
Supplementary Figure 44. Photovoltaic parameters statistical distribution of PSCs using PATPA and PATPA:TATPA (PATPA-SAB) as hole-selective contacts 55
Supplementary Figure 45. Photovoltaic parameters statistical distribution of 1.68-eV PSCs ($Cs_{0.21}FA_{0.74}MA_{0.05}Pb(I_{0.81}Br_{0.14}Cl_{0.05})_3$) utilizing SAM or SAB as the hole-selective contact 56
Supplementary Figure 46. Device performance decay for 140 days stored in dark under N_2 protection at room temperature 57

Supplementary Figure 47. MPPT Stability results of PSCs based on SAM and SAB. The cells are under simulated 1-sun illumination and held at 70 ºC and 85 ºC 58
Supplementary Figure 48. Photographs and a cross-section sketch showing our device that has been double-encapsulated by PIB and UV-cured glue 59
Supplementary Figure 49. EQE_{EL} results for aged PSCs using SAM and SAB as hole-selective contacts after thermal cycling 60
Supplementary Figure 50. Stability of PSCs based on MPA-CPA and SAB 61
Supplementary Figure 51. Recent reports on damp heat (A) and thermal cycling (B) stabilities based on IEC61215:2016 protocols 62
Supplementary Figure 52. Surface SEM images and EDS spectra of the perovskite films upon annealing at 100 ºC for 50 min 65
Supplementary Figure 53. XPS spectrum of the perovskite film containing 8% MACl in its precursor, and annealed at 100 ºC for 50 min 66
Supplementary Note 1. The formation of carbocation intermediates indicated by the methoxylation of decomposed TATPA using deuterated methanol 8
Supplementary Note 2. HRMS and NMR characterizations of the Friedel-Crafts alkylation mechanism 16
Supplementary Note 3. General applicability of SAB approach 22
Supplementary Note 4. Analysis of 2PACz SAM structure 29
Supplementary Note 5. Analysis of SAB structure 33
Supplementary Note 6. Analysis of area density after thermal cycle stress 36
Supplementary Note 7. TRPL and PLQY characterization to SAB on perovskite 41
Supplementary Table 1. Device parameter statistics of 20 individual PSCs based on pristine 2PACz SAM 50
Supplementary Table 2. Device parameter statistics of 20 individual PSCs based on SAB 51
Supplementary Table 3. Summary of stability data for PSCs under damp-heat conditions (85°C and 85% relative humidity) 63
Supplementary Table 4. Summary of stability data for PSCs under thermal cycling from -40°C to 85°C 64
Supplementary References 67

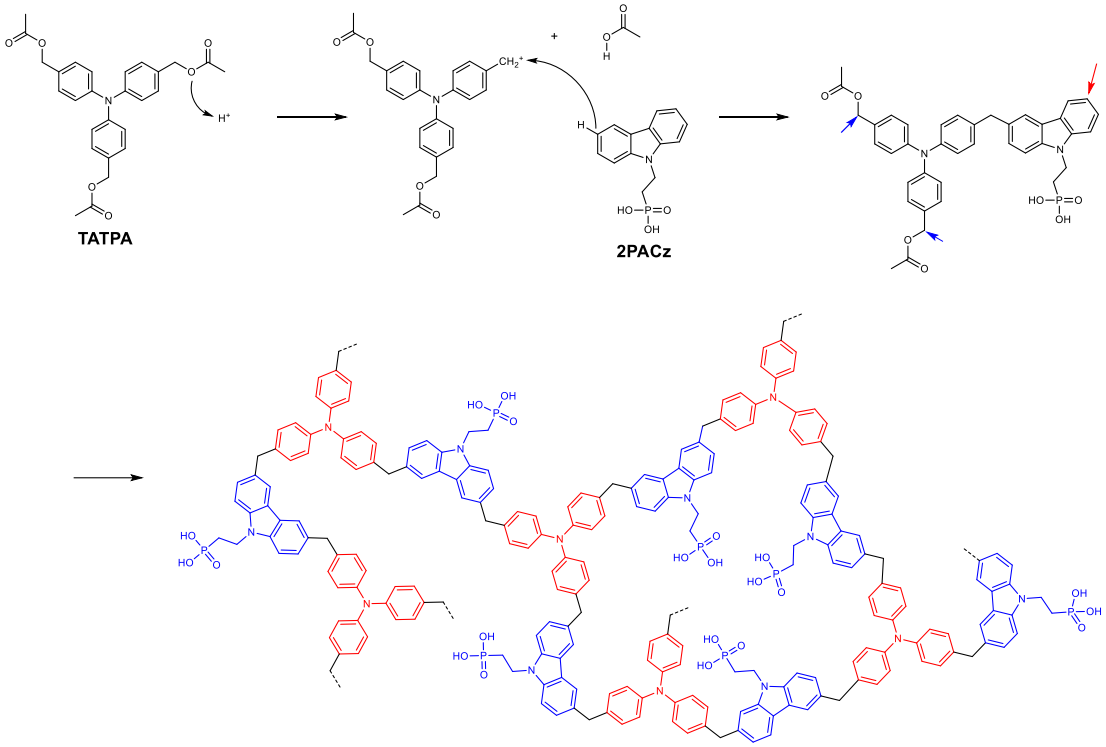

Supplementary Figure 1. Schematic diagram of SAB structure and formation. *Carbocation mechanism for the in-situ coupling reaction between TATPA and 2PACz. The reaction between TATPA and 2PACz can be considered typical multi-functional non-linear condensation reaction due to the reaction moieties being 3:2, instead of 2:2, as indicated in the figure with blue and red arrow.*

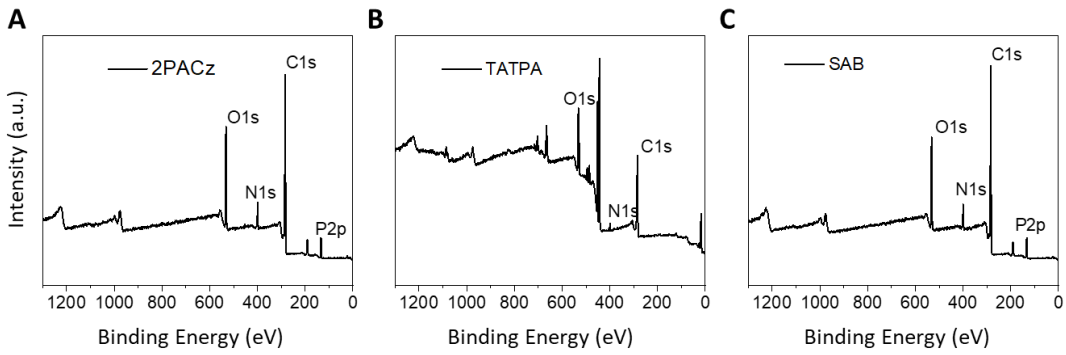

Supplementary Figure 2. X-ray photoelectron spectroscopy (XPS) full spectra of 2PACz, TATPA, and SAB.

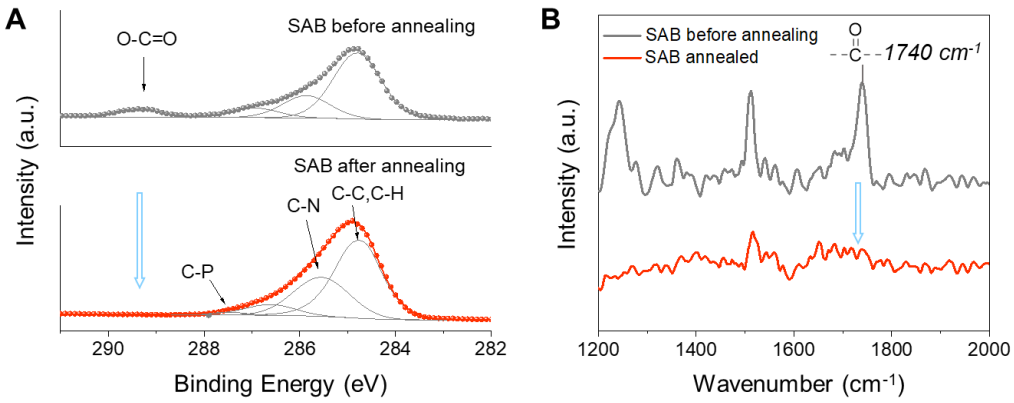

Supplementary Figure 3. Characterizations of SAB before and after annealing. A*, XPS and* ***B****, ATR-FTIR spectra of SAB before and after thermal annealing. The solid line shows the fit to the data and the dotted lines show the components thereof fit a Gaussian distribution.*

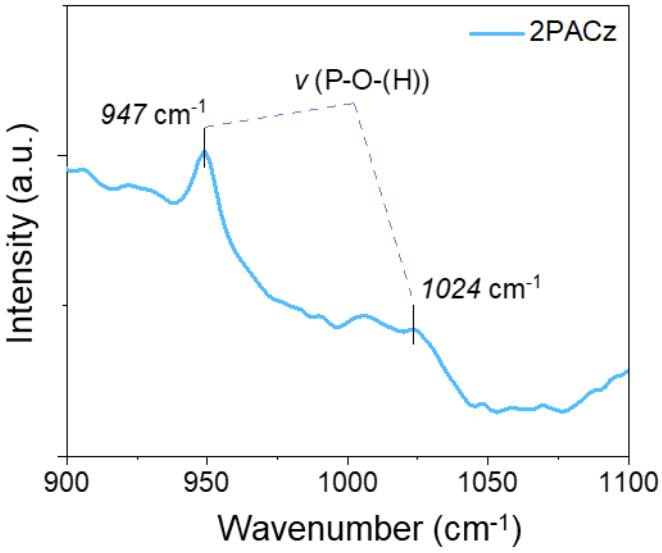

Supplementary Figure 4. Attenuated Total-reflective Fourier Transform Infrared (ATR-FTIR) Spectroscopy spectra of 2PACz film.

Supplementary Note 1,

The formation of carbocation intermediates indicated by the methoxylation of decomposed TATPA using deuterated methanol

Carbocations are highly electrophilic and undergo substitution reactions with methanol, forming methoxylated compounds[38]. To verify the generation of carbocation intermediates from decomposed TATPA, we exploited methoxylation using deuterated methanol (CD_3OD) as probes. TATPA with 5% 2PACz was cast on substrates and heated to 100°C for 10 minutes to initiate film decomposition. The resulting solids were dissolved in CD_3OD and subsequently heated at 50°C for 2 hours to promote methoxylation. The reaction mechanism is depicted in **Supplementary Figure 5**.

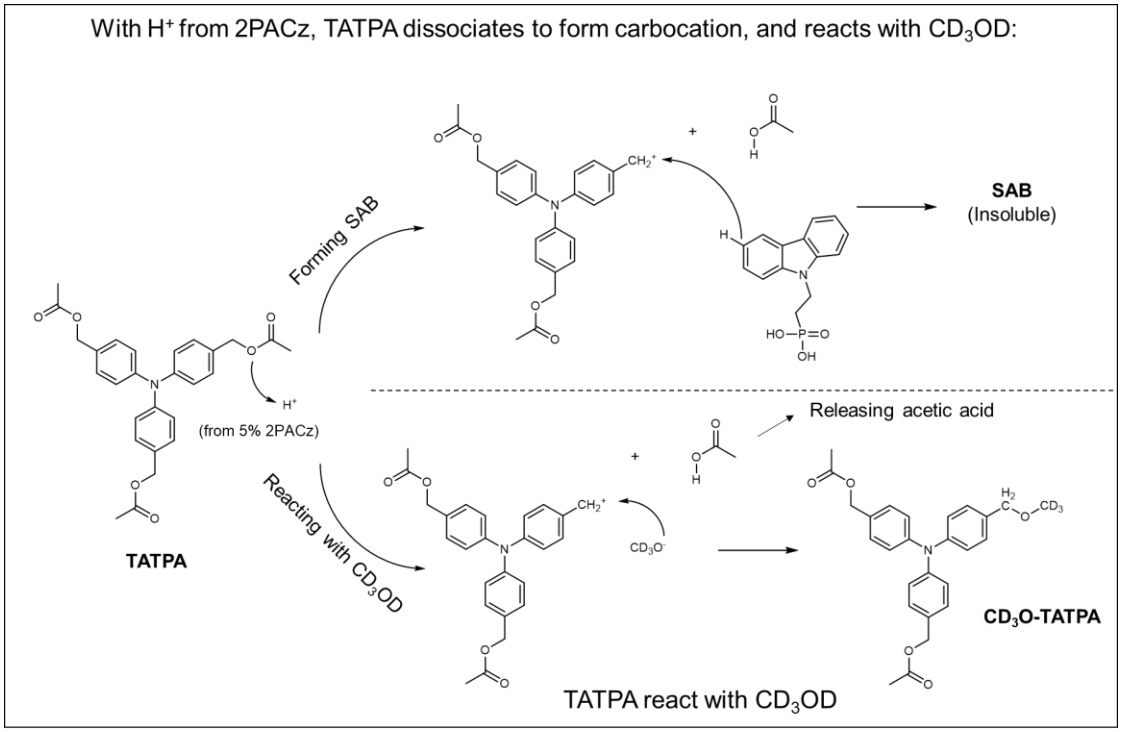

Supplementary Figure 5. Reaction mechanism of H^+ catalyzed methoxylation of TATPA with CD_3OD.

We utilized ^{1}H NMR to monitor the reaction, with results presented in Supplementary **Figure 6** showing a new peak at $\delta = 4.39$ ppm, corresponding to the H' of methoxylated product, CD_3O-TATPA.[38]

Additionally, a shift for the α-hydrogen of acetic acid (CH_3COOH, δ = 1.97 ppm) emerged post reaction. These findings support the formation of a carbocation intermediate and acetic acid as a by-product. Combining these results, we reason that 2PACz effectively initiates the decomposition of TATPA, generating reactive intermediates for the subsequent reactions detailed below.

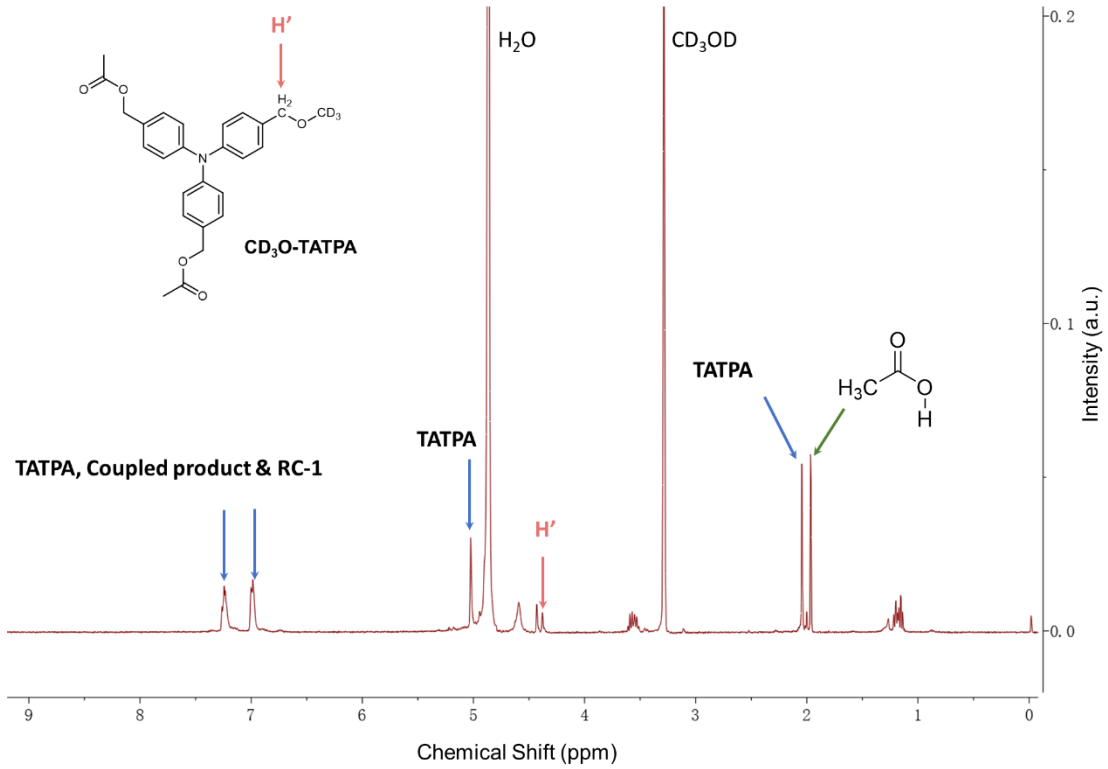

Supplementary Figure 6. ^{1}H-NMR spectra of the reacted mixture of TATPA and CD_3OD*, containing 5% 2PACz to trigger the methoxylation reaction.*

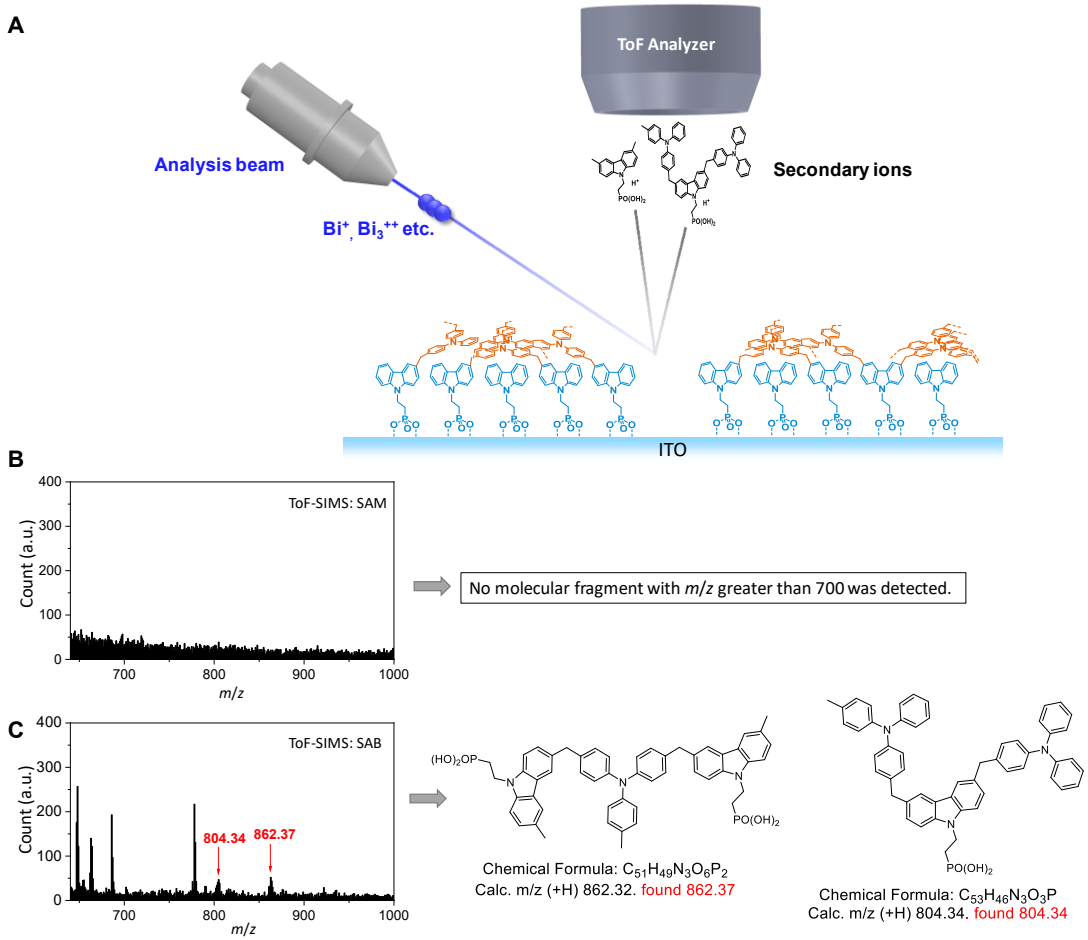

Supplementary Figure 7. ToF-SIMS results of SAB. ***A****, Schematic diagram of ToF-SIMS characterization of SAB,* ***B*** *and* ***C****, ToF-SIMS spectra of SAM and SAB on substrates, respectively. In panel* ***C****: two possible molecular fragments from SAB are identified, corresponding to those observed in the ToF-SIMS spectra. ToF-SIMS is usually attributed to hard ionization techniques, which typically generate a larger number of atomic fragments and fewer molecular fragments. As a result, the isotopic peaks for these molecular fragments are often difficult to visualize due to their relatively low signal intensity. This limitation makes it challenging to observe the isotopic distribution of molecular ions clearly in ToF-SIMS spectra, and as such, these peaks are not shown here*[68]*. The presence of isotopic peaks was confirmed through HRMS analysis, as illustrated in* ***Supplementary Figures 14, 22,*** *and* ***23****.*

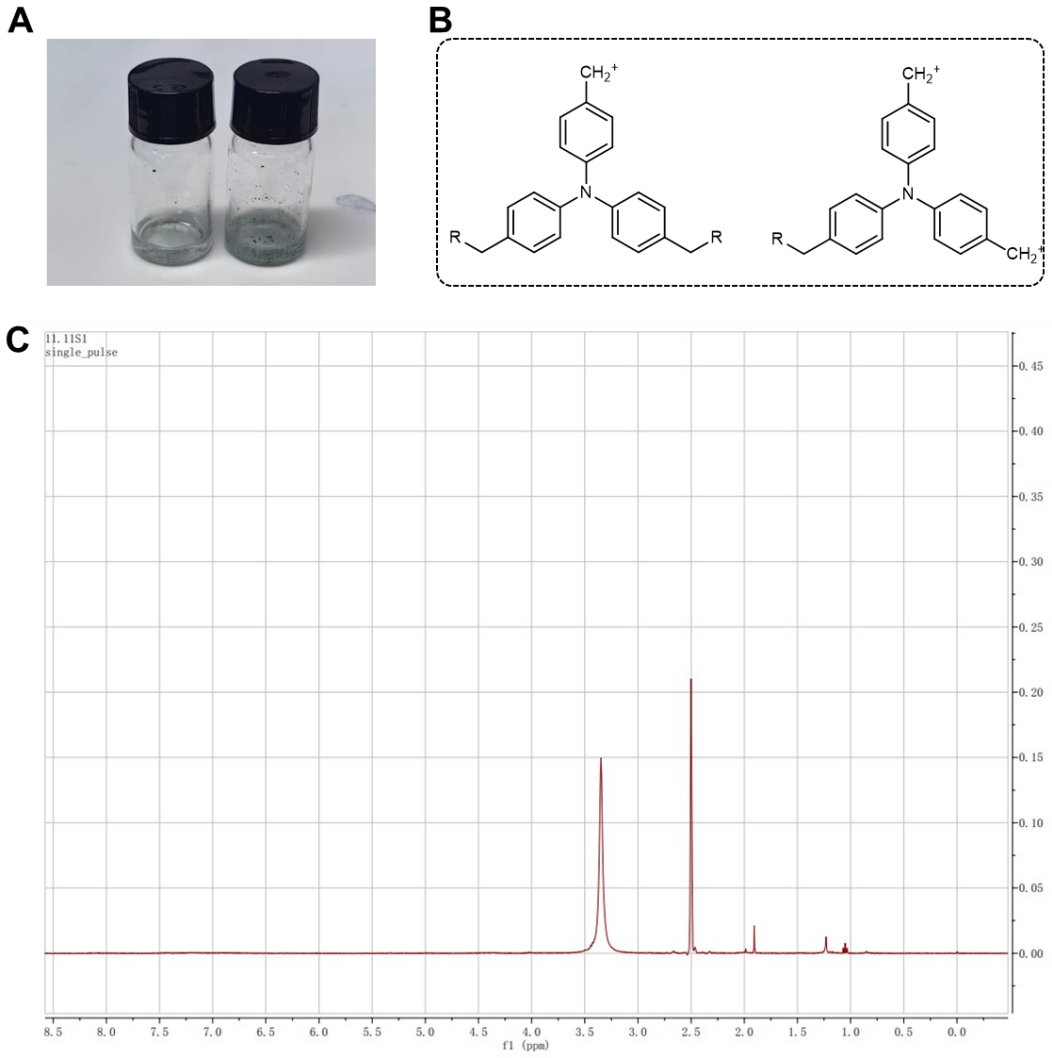

Supplementary Figure 8. Characterization of the cross-linked SAB. ***A****, photographs of scratched SAB crosslinked polymer in dimethyl sulfoxide (DMSO, left) and chlorobenzene (CB, right). They are placed on a 110 °C hotplate.* ***B****, chemical structures of possible intermediate phase that show greenish color, and* ***C****, ^{1}H NMR spectrum of the SAB polymer in DMSO-d6.*

The scratched sample was sent to measure ^{1}H NMR in DMSO-d6 and we observed no signal in the low-field region, indicating the fact that the coupling reaction between 2PACz and TATPA is very efficient at 1:1 weight ratio – almost all the precursor monomers are consumed to form the robust SAB network.

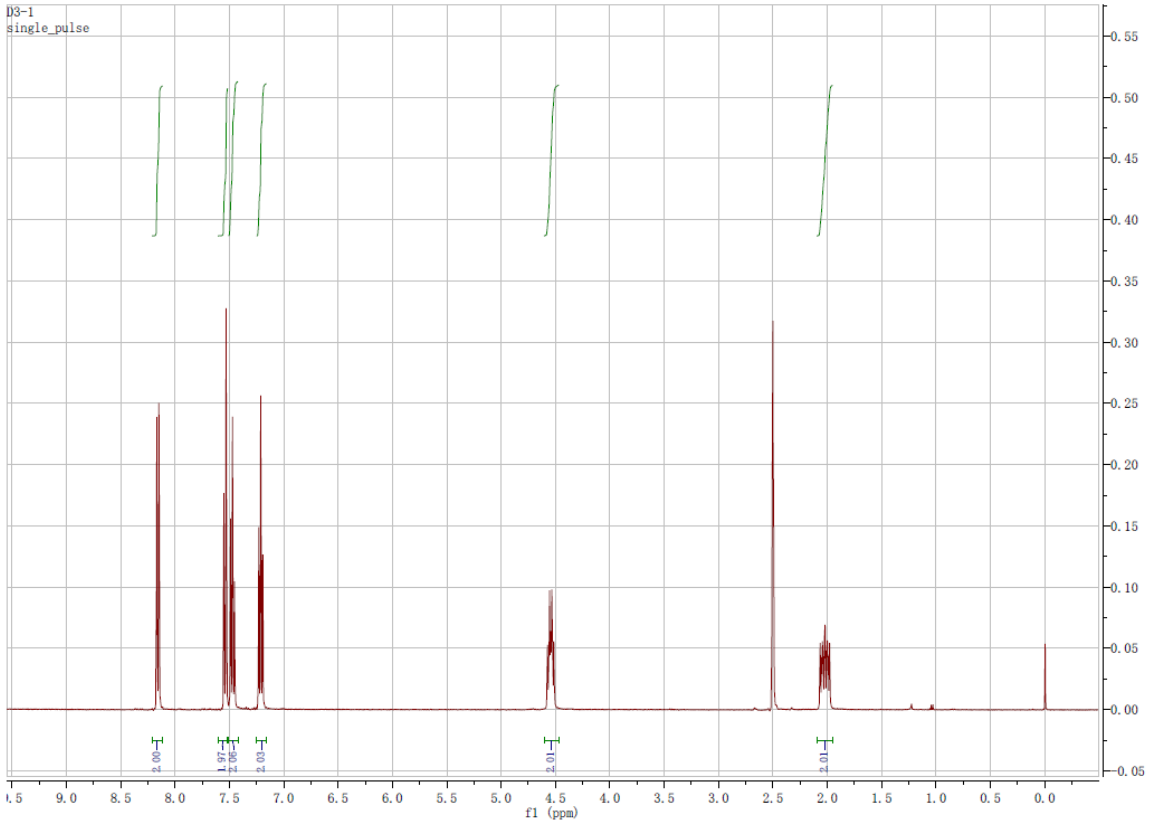

Supplementary Figure 9. ^{1}H NMR spectrum of 2PACz.

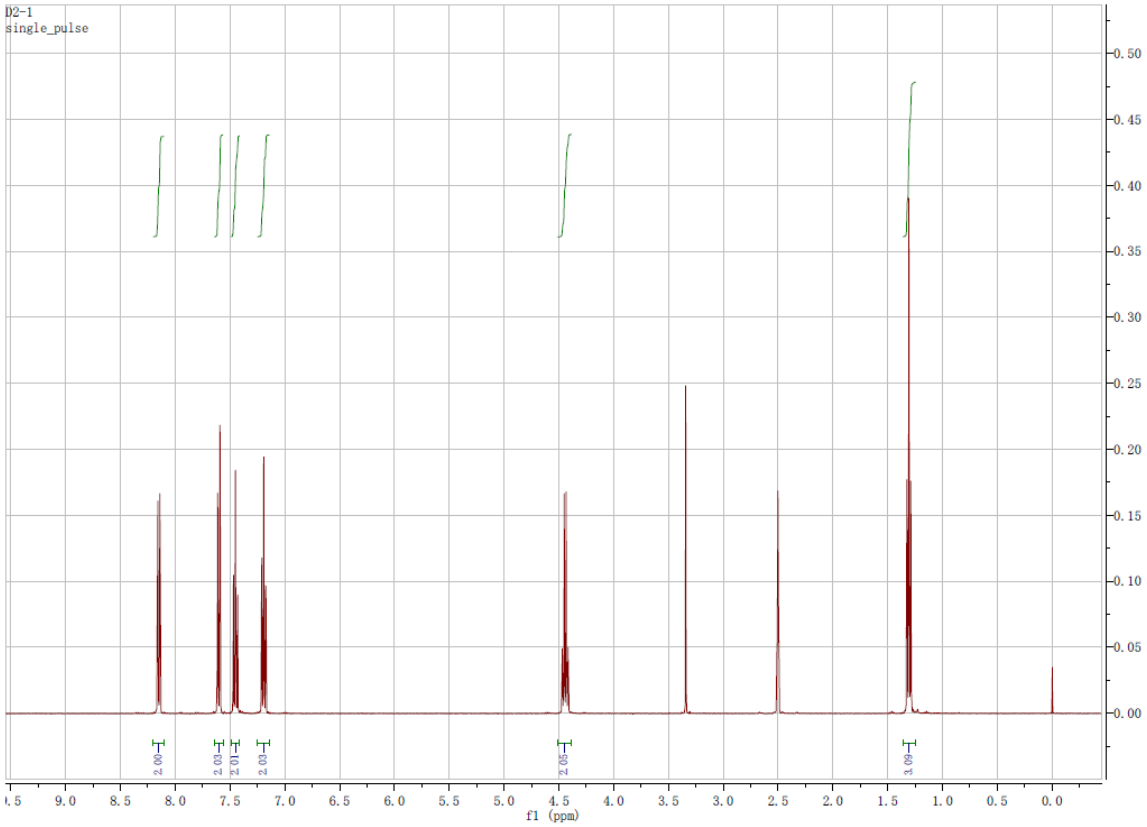

Supplementary Figure 10. ^{1}H NMR spectrum of NECz.

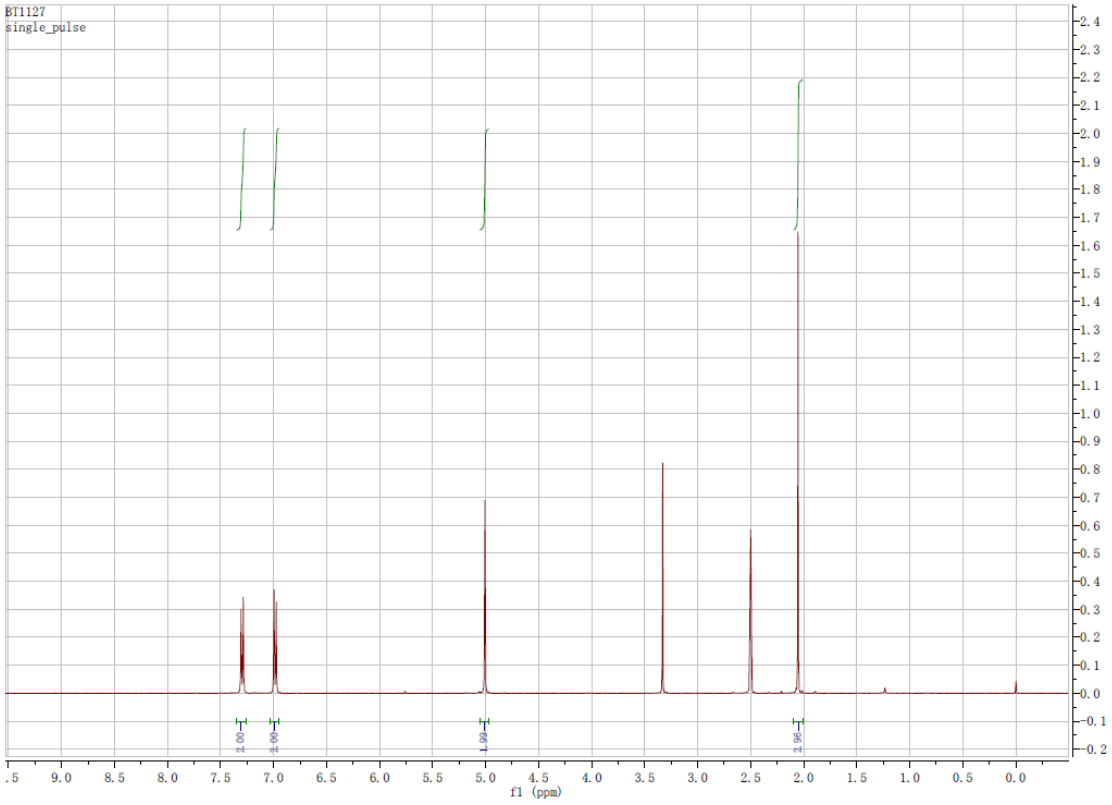

Supplementary Figure 11. ^{1}H NMR spectrum of TATPA.

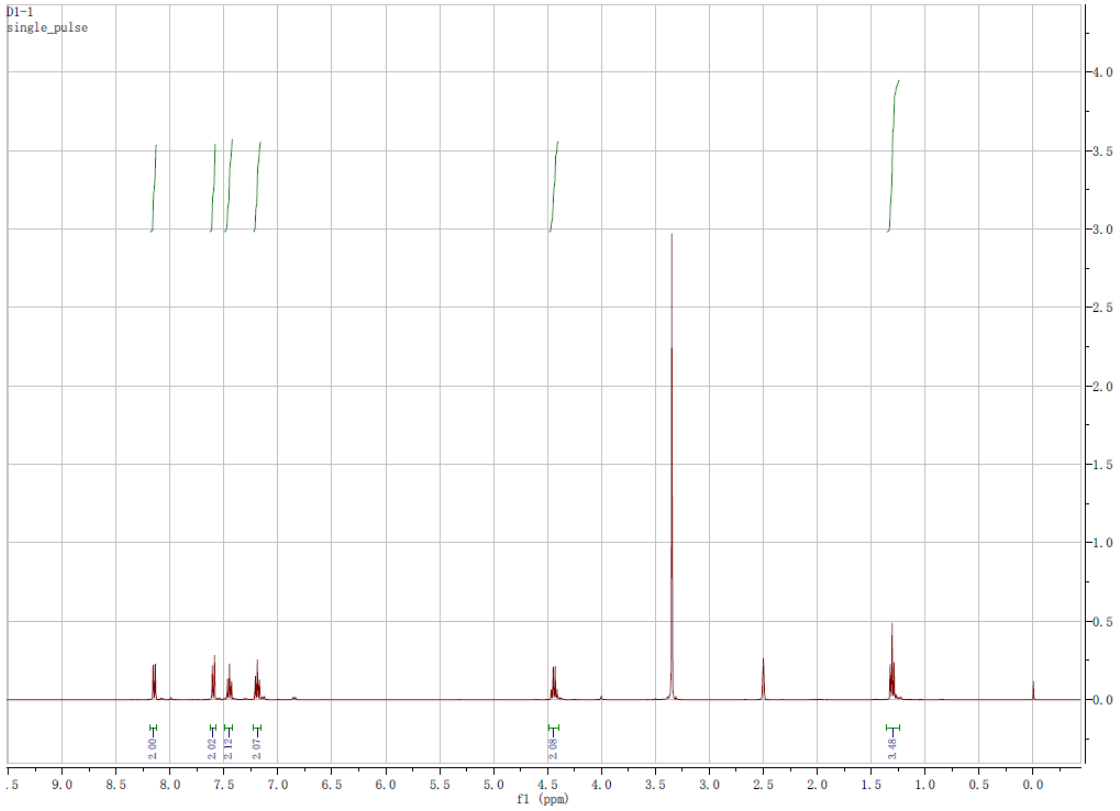

Supplementary Figure 12. ^{1}H NMR Spectrum of NECz:TATPA:2PACz equals to 100:10:1.

Supplementary Note 2

HRMS and NMR characterizations of the Friedel-Crafts alkylation mechanism

We synthesis a less reactive variant of TATPA, designated DTBA, containing only one –COOMe group per molecule, as illustrated in Supplementary **Figure 13**. Unlike forming a polymerized network, the reaction with 2PACz produces a triphenylamine-substituted small molecule, DTBA-2PACz, soluble in organic solvents for chemical analysis. Films containing 2PACz and DTBA were cast on glass substrates, annealed at 100°C for 10 minutes, then rinsed to prepare for high-resolution mass spectrometry (HRMS) analysis. It confirmed the presence of DTBA-2PACz in both positive and negative ion modes, with m/z values matching its predicted figures ($C_{56}H_{52}N_3O_3P$, -H: Calculated: 844.3668, Observed: 844.3678; +H; Calculated: 846.3825, Observed: 846.3819, **Supplementary Figure 14**). We also observed in **Supplementary Figure 14** that the presence of isotopic peaks offers further evidence of the alkylated product between 2PACz and DTBA.

Then, we utilized ^{1}H-^{1}H COSY and C-H HSQC to confirm the C-C coupled product structure. In the ^{1}H NMR analysis, we identified a new singlet peak at δ = 4.00 ppm assigned to methylene bridge protons, indicative of the Friedel-Crafts alkylation (**Supplementary Figure 15**). C-H HSQC measurements on DTBA-2PACz confirmed this assignment, revealing a C–H coupling peak at δ = 4.00 ppm for ^{1}H and δ = 40.97 ppm for ^{13}C (**Supplementary Figure 16**), which represents the correlation between the methylene carbon and its attached protons[38].

We proposed that Friedel-Crafts alkylation led to the triphenylamine substitution on carbazoles at the C3 or C6 positions. In the ^{1}H-^{1}H COSY spectra, cross-peaks associated with the methylene protons were identified at δ 7.15 ppm and 8.03 ppm, along with the self-coupling peak at δ = 4.00 ppm (**Supplementary Figure 17**). The cross-peaks, when compared with 1D ^{1}H NMR data, were attributed to interactions with neighboring protons: H-c from the triphenylamine unit and H-b from the carbazole

group. This pattern confirms the direct coupling between 2PACz and triphenylamine units, driven by the electrophilic attack of the carbocation intermediate.

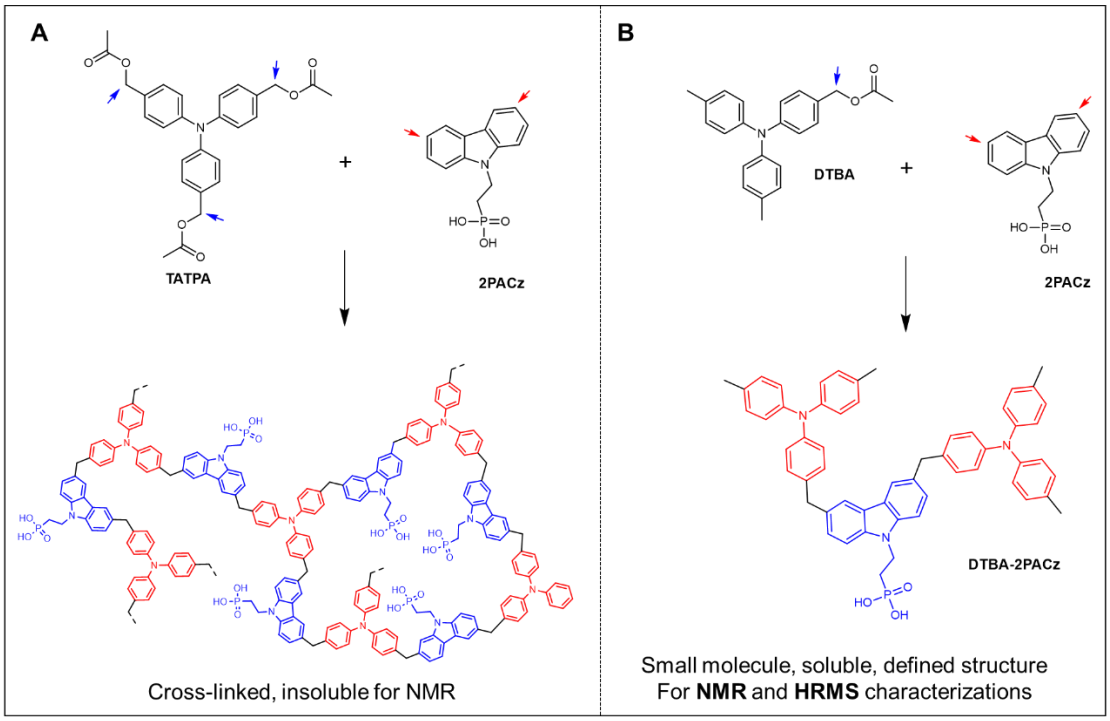

Supplementary Figure 13. Design rationale of DTBA-2PACz. ***A***, ***B***, *Chemical structures of TATPA (**A**), DTBA, and DTBA-2PACz (**B**). The single functional group, –COOMe, on DTBA leads to the formation of a small-molecule coupling product rather than a cross-linked network.*

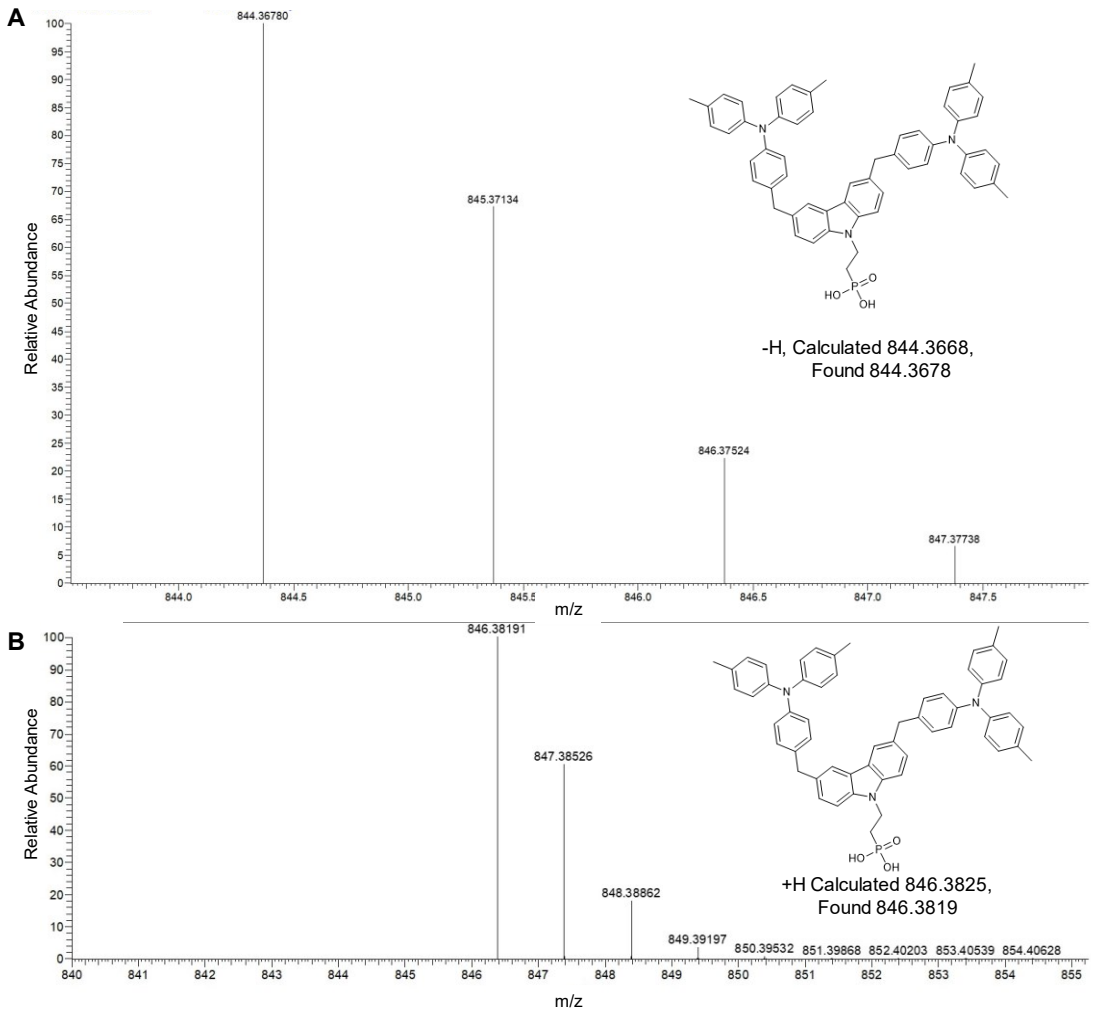

Supplementary Figure 14, High-Resolution Mass Spectroscopy (HRMS) spectra of DTBA-2PACz, *-H mode (A) and +H mode (B).*

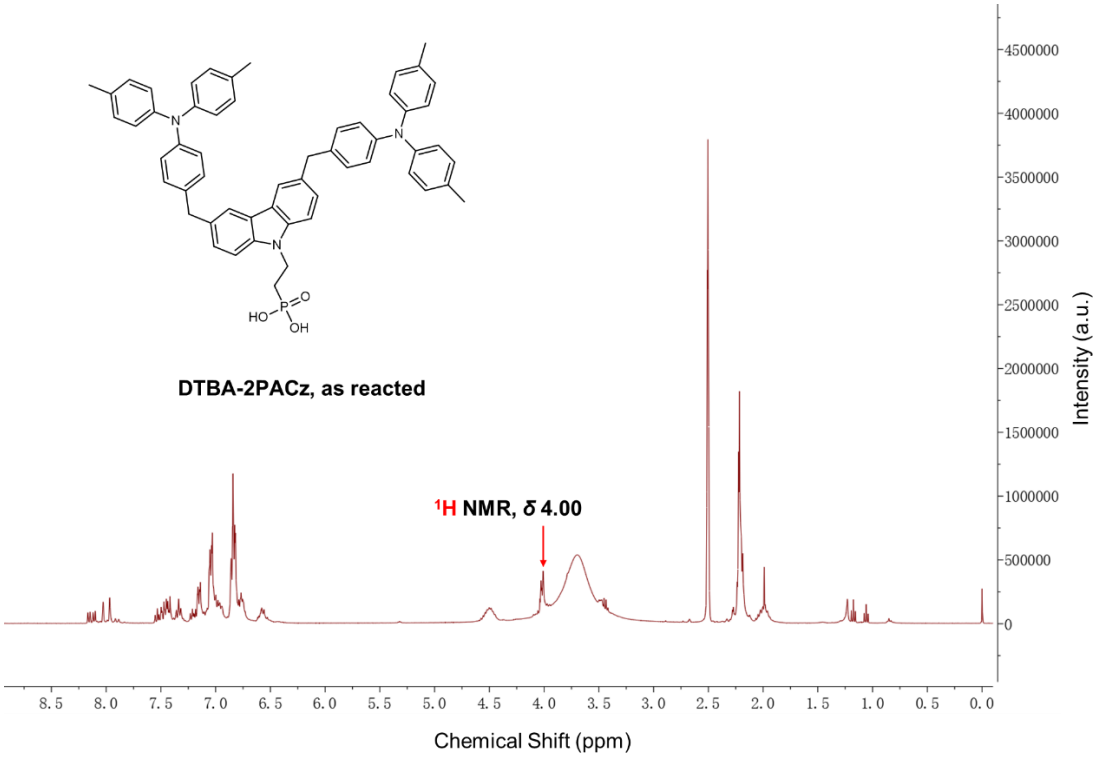

Supplementary Figure 15, 1H-NMR spectra of as-reacted DTBA-2PACz.

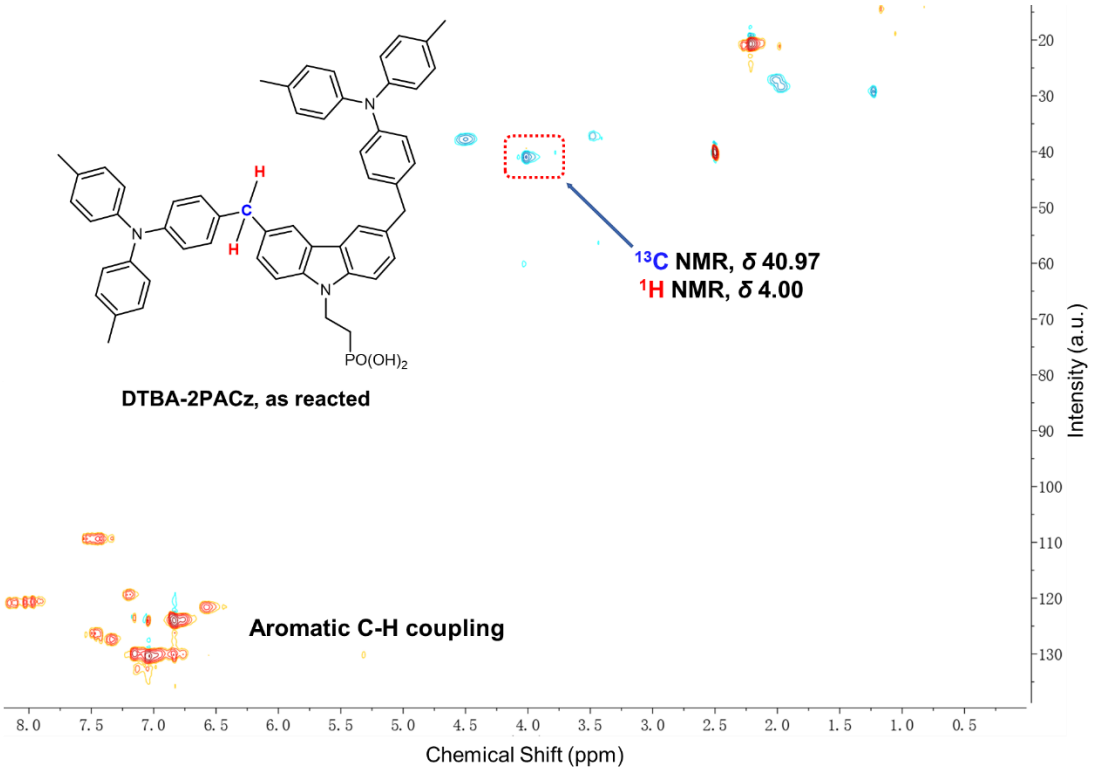

Supplementary Figure 16, C-H Heteronuclear single quantum coherence (HSQC) spectra of DTBA-2PACz.

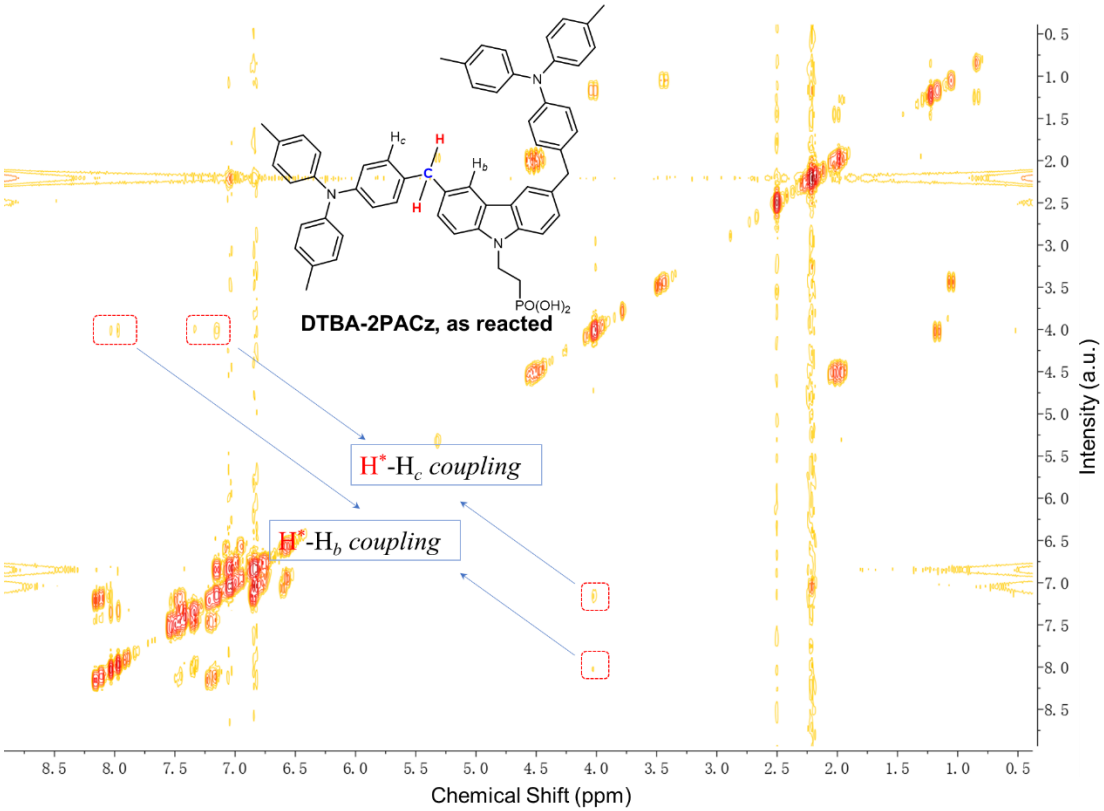

Supplementary Figure 17, ^{1}H-^{1}H correlation spectroscopy (COSY) NMR spectra of DTBA-2PACz, *the small molecule counterpart of SAB. DTBA-2PACz is highly soluble in DMSO-d6 for NMR characterizations.*

Supplementary Note 3

General applicability of SAB approach

Note 3-1, New alkylating agents to form SAB: We synthesized a new alkylating agent, bisTATPA, featuring a linked triphenylamine core that offers a larger π-plane compared to TATPA.[38] The structure of bisTATPA and a potential SAB formation and coupling mechanism are both depicted in **Supplementary Figure 18**.

We deposited bisTATPA atop the 2PACz SAM using the same procedure as for TATPA to construct the SAB. ATR-FTIR revealed a characteristic disappearance of the carbonyl peak after thermal annealing (**Supplementary Figure 19**), suggesting that the underlying phosphonic acids could also decompose bisTATPA to produce reactive carbocations.

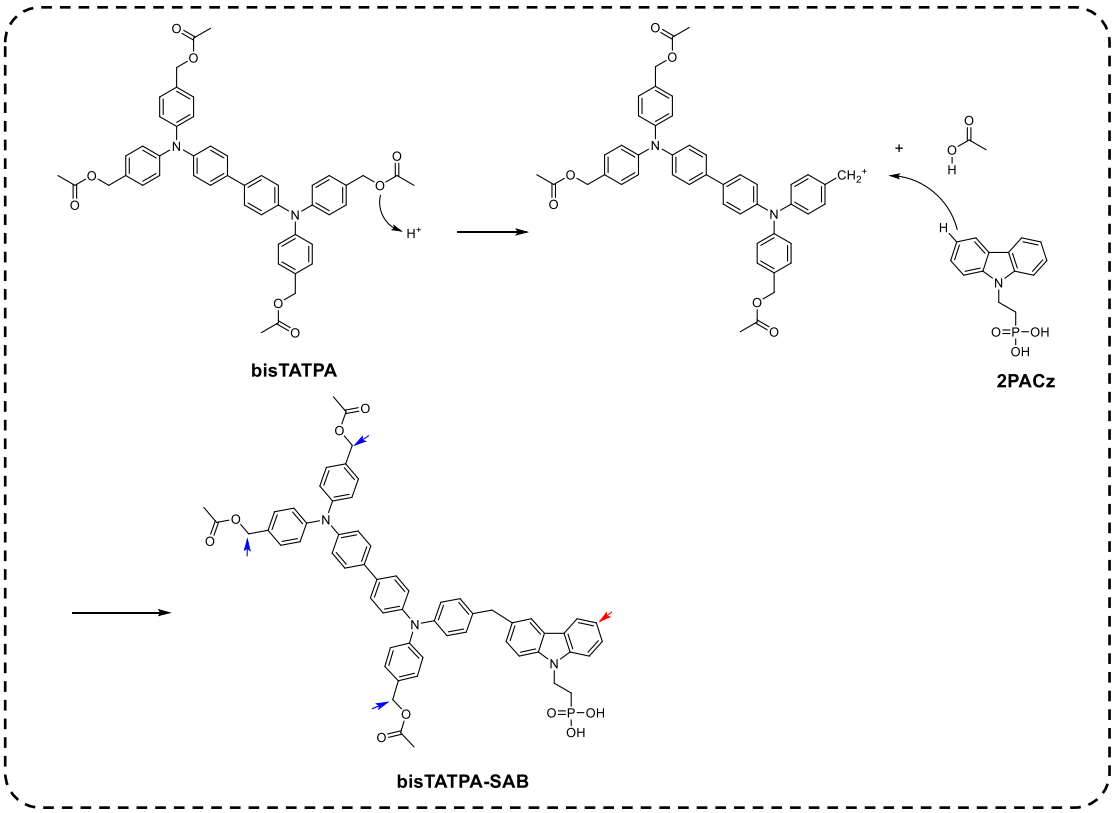

Supplementary Figure 18. Chemical structure of bisTATPA and SAB formation mechanism between 2PACz and bisTATPA.

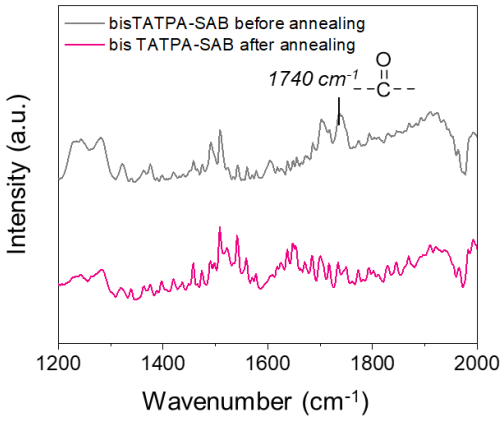

Supplementary Figure 19, ATR-FTIR spectra of bisTATPA and 2PACz based SAB before and after thermal annealing.

Note 3-2, New SAM-forming molecules: We also recognize the need to demonstrate the applicability of the SAB approach to other molecular hybrid systems. In principle, TATPA should react with different carbazole- or triphenylamine-based phosphonic acids where the *para*-position relative to the nitrogen atom is unsubstituted, allowing for electrophilic attack by the carbocation. We have therefore investigated two representative SAM-forming molecules: one based on carbazole, namely 4PACz[69], and the other on triphenylamine, referred to as PATPA (Supplementary **Figure 20**).[70] TATPA and various SAB bilayers were prepared using the same protocol as for the 2PACz-based system.

Prior to thermal annealing, ATR-FTIR spectra showed that the carbonyl peak of TATPA at 1740 cm^{-1} remained intact (**Supplementary Figure 21**). Upon annealing, decomposition of TATPA became evident, indicating the potential of 4PACz and PATPA as proton donors that catalyze Friedel-Crafts alkylation. Nonetheless, the extent of this reaction varied, as residual carbonyl signals were still detectable in the 4PACz-based system. To demonstrate SAB formation with various SAM-forming molecules, films containing 4PACz/PATPA and DTBA (**Supplementary Figure 13**) were deposited on glass substrates and annealed at 100°C for 10 minutes. Post-annealing, the films were rinsed to prepare samples for HRMS analysis. **Supplementary Figure 22** and **Supplementary Figure 23** confirmed the C-C coupling between 4PACz or PATPA and DTBA, with mass spectral peaks aligning with predictions of their reaction products.

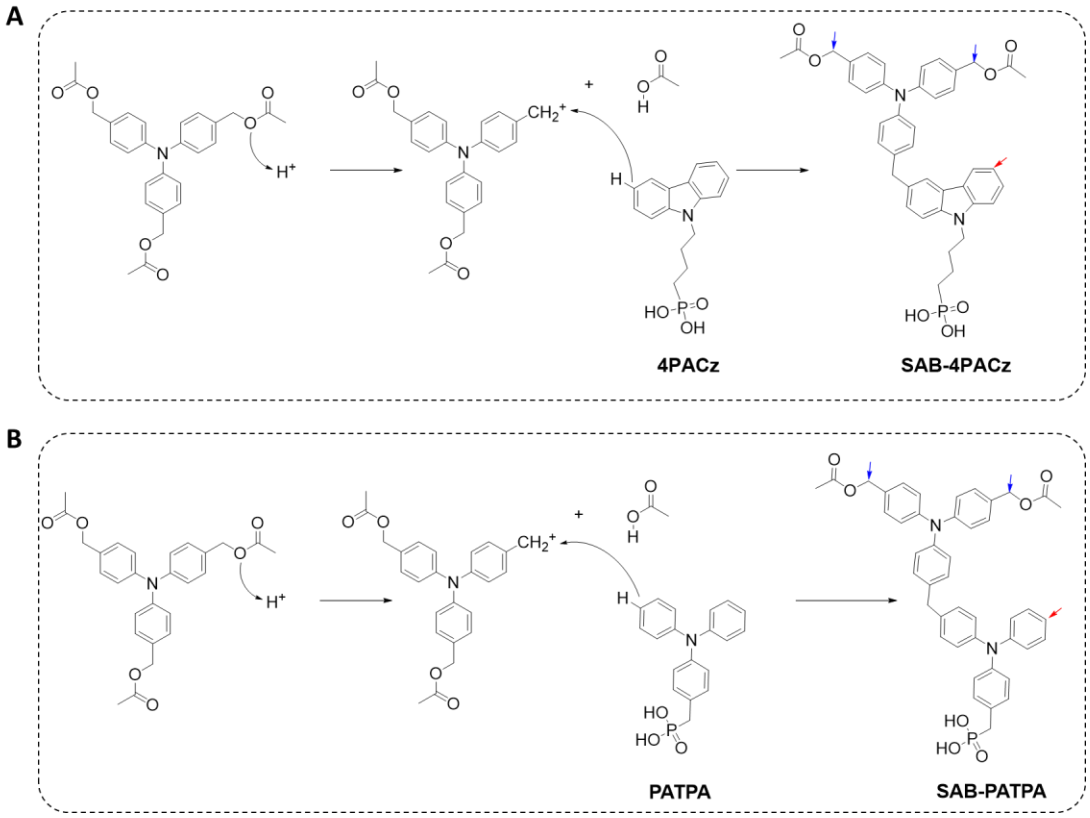

Supplementary Figure 20. Formation mechanism of SABs based on 4PACz and PATPA. ***A*** *and* ***B****, the chemical structures of 4PACz and PATPA, respectively, along with the mechanisms of SAB formation involving these compounds.*

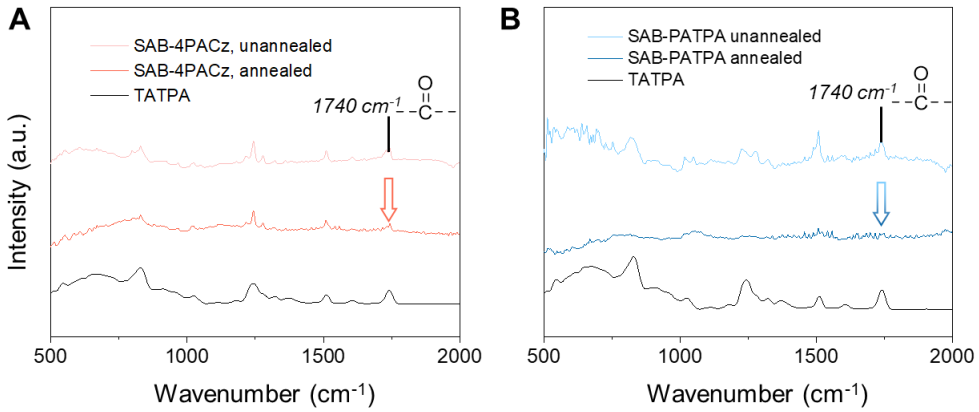

Supplementary Figure 21. ATR-FTIR spectra of TATPA-based SABs before and after thermal annealing*, featuring bottom layers of 4PACz and PATPA.*

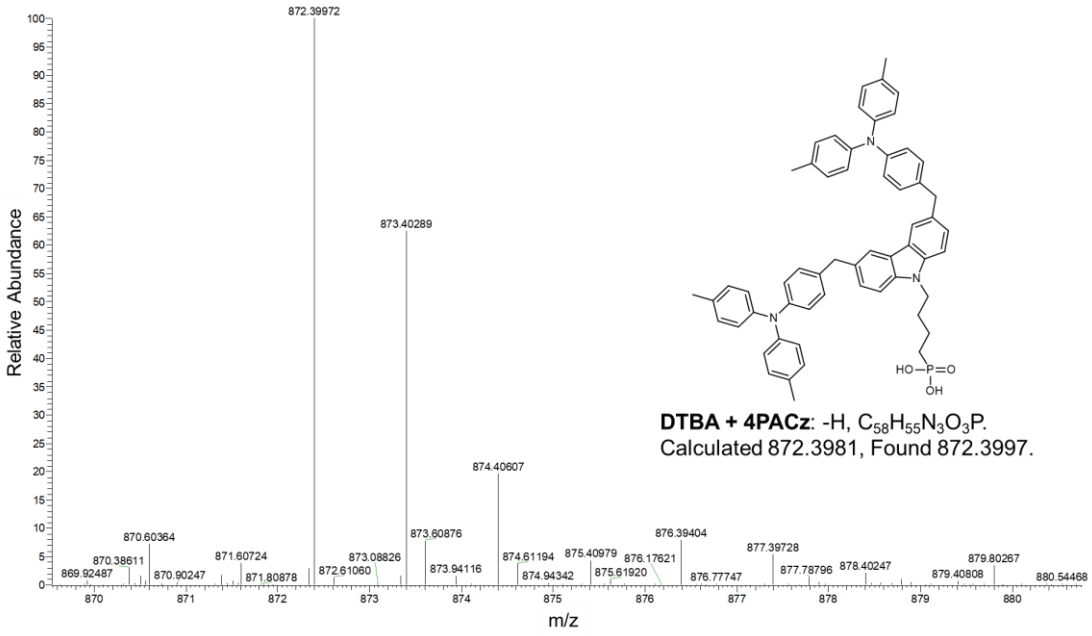

Supplementary Figure 22. HRMS spectra of the coupled product between DTBA and 4PACz.

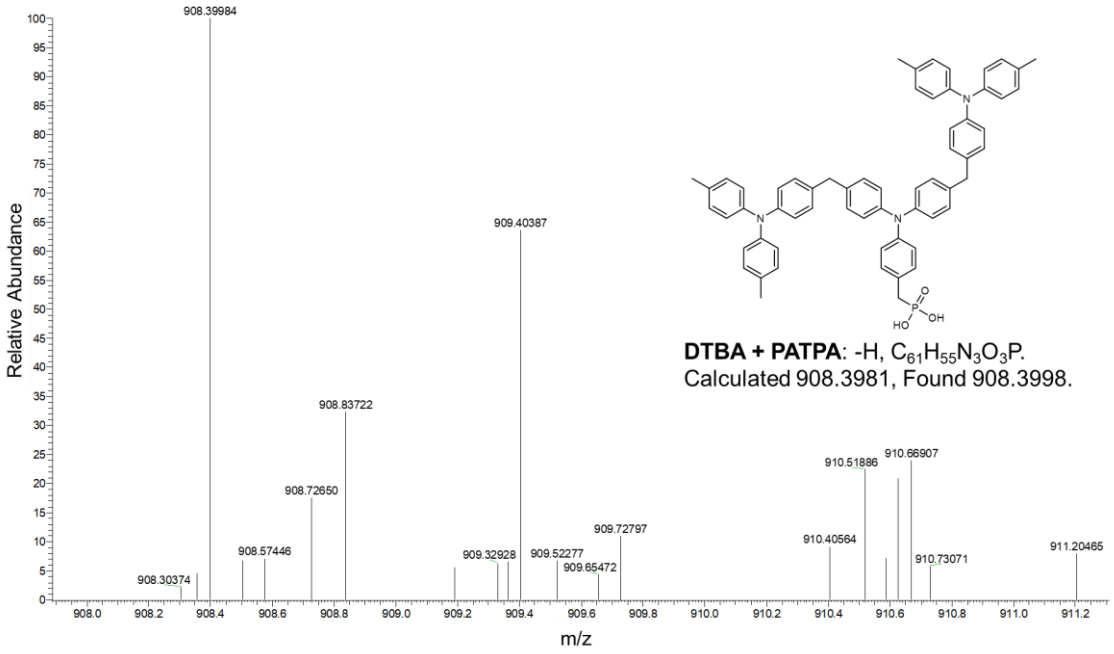

Supplementary Figure 23. HRMS spectra of the coupled product between DTBA and PATPA.

Supplementary Note 4

Analysis of 2PACz SAM structure

As shown in **Supplementary Fig. S24**, for pristine 2PACz SAM at 0.5 mg mL^{-1} precursor concentration (equaling to that in best performing PSCs), the weak peak at q_z = 0.415 $Å^{-1}$ as marked in the black square indicated that 2PACz based SAM is not precisely 'monolayer'. There exists a small amount of 2PACz stacked at the out-of-plane direction, with a lattice distance of 1.51 nm. The diffraction peak at q_{xy} = 1.56 $Å^{-1}$ at the in-plane direction prove that the aggregation of 2PACz is preferably 'vertical' to the substrate, as marked in yellow. Meanwhile, the diffraction ring diffuses slightly toward q_z direction (marked in red), proving that the 2PACz molecules are not 100% 'vertical', instead, there exist certain 'tilt' for 2PACz on ITO substrate, as marked in the red square.

To observe assemble trend of 2PACz, we increased the precursor concentration from 0.5 mg mL^{-1} to 5 mg mL^{-1} and measured GIWAXS. As shown in **Supplementary Figure 25**, the same but stronger peak at q_z = 0.415 $Å^{-1}$ (marked in black square) emerged at higher concentration 2PACz coated on ITO, proved similar out-of-plane stacking exists as compared with the 2PACz at lower concentration. The intensive scattering dot emerged at q_{xy} = 1.56 $Å^{-1}$ (marked in yellow square, identical q value compared with low concentration sample), provided pronounced evidence that 2PACz molecules are preferably 'edge-on', where the phosphonic binding group is attached to ITO and the aliphatic carbazole 'tail' is exposed to the perovskite side, as illustrated also in **Fig. 3i**.

We note that at higher concentration, 'tilt' of the 2PACz molecules (as shown in **Supplementary Figure 25**) does not seem exist since the scattering peak at q_{xy} = 1.56 $Å^{-1}$ is a dot instead of an arc. (yellow square)

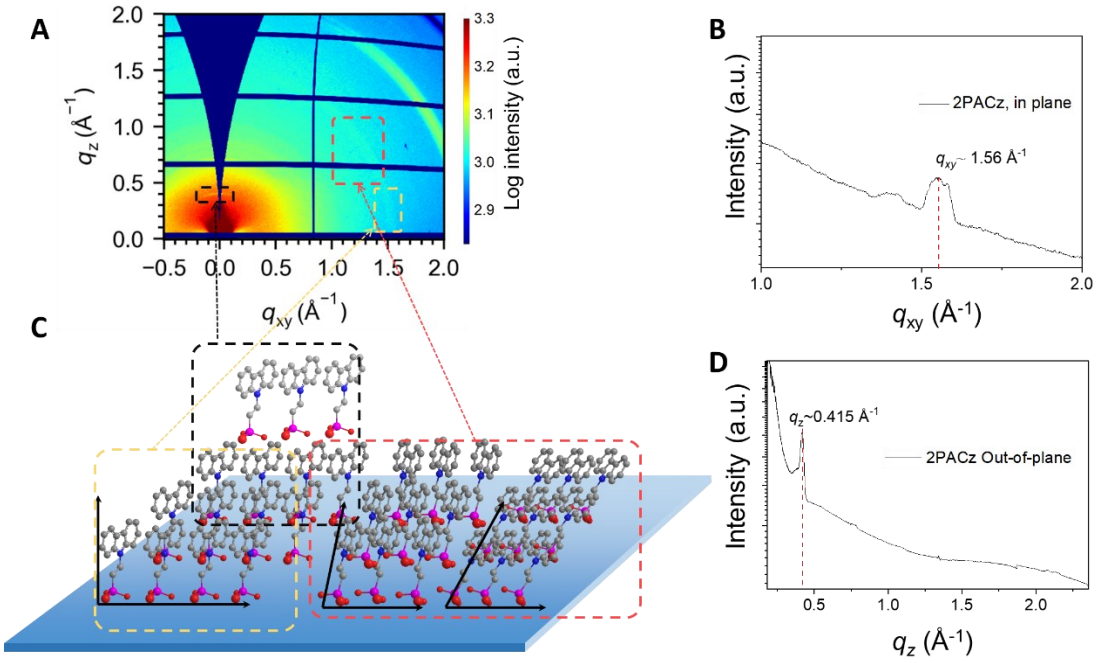

Supplementary Figure 24. Structural characterization of 2PACz SAM. *A, 2D GIWAXS pattern and illustrative aggregation structure of pristine 2PACz coated on ITO surface. The precursor concentration is adjusted to the same that corresponding PSC devices yielding best optimized efficiency (0.5 mg/mL).* ***B****, and* ***C****, integration of the diffractions along q_{xy} direction and q_z direction.* ***D****, illustrative sketch showing the aggregation of low-concentration 2PACz coated on ITO surface.*

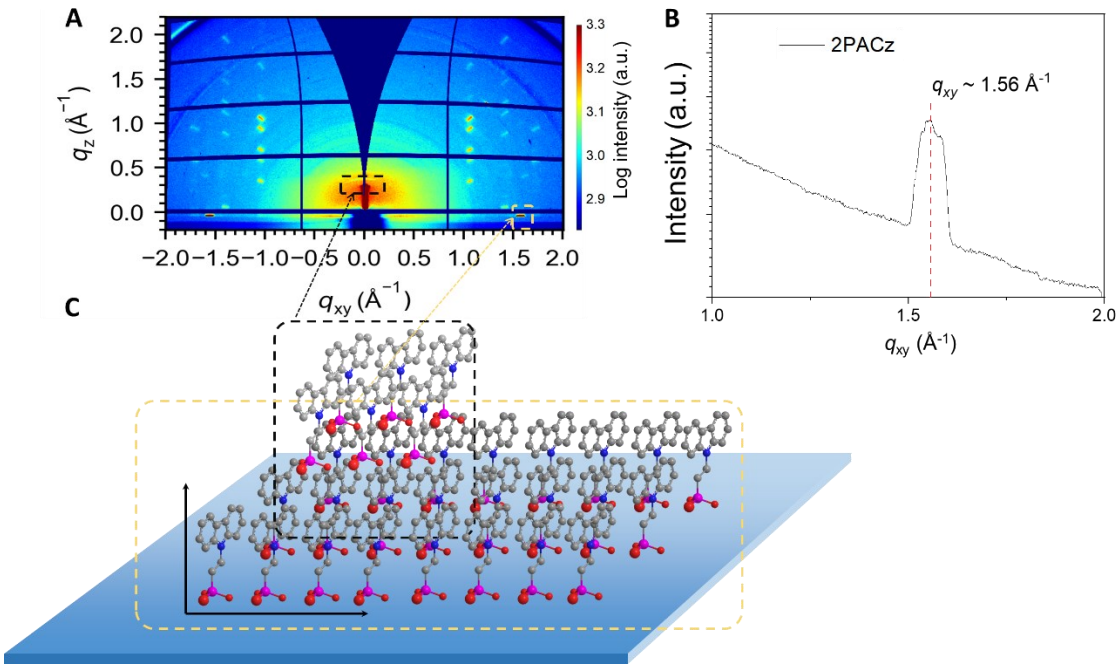

Supplementary Figure 25. Structural characterization of 2PACz SAM at increased precursor concentration. ***A****, 2D GIWAXS pattern and illustrative aggregation structure of pristine 2PACz coated on ITO surface. The precursor concentration is increased to 5 mg/mL to better visualize the aggregation structure of pristine 2PACz on ITO substrate.* ***B****, integration of the diffractions along in-plane direction.* ***c****, illustrative sketch showing the aggregation of high-concentration 2PACz coated on ITO surface (5 mg/mL).*

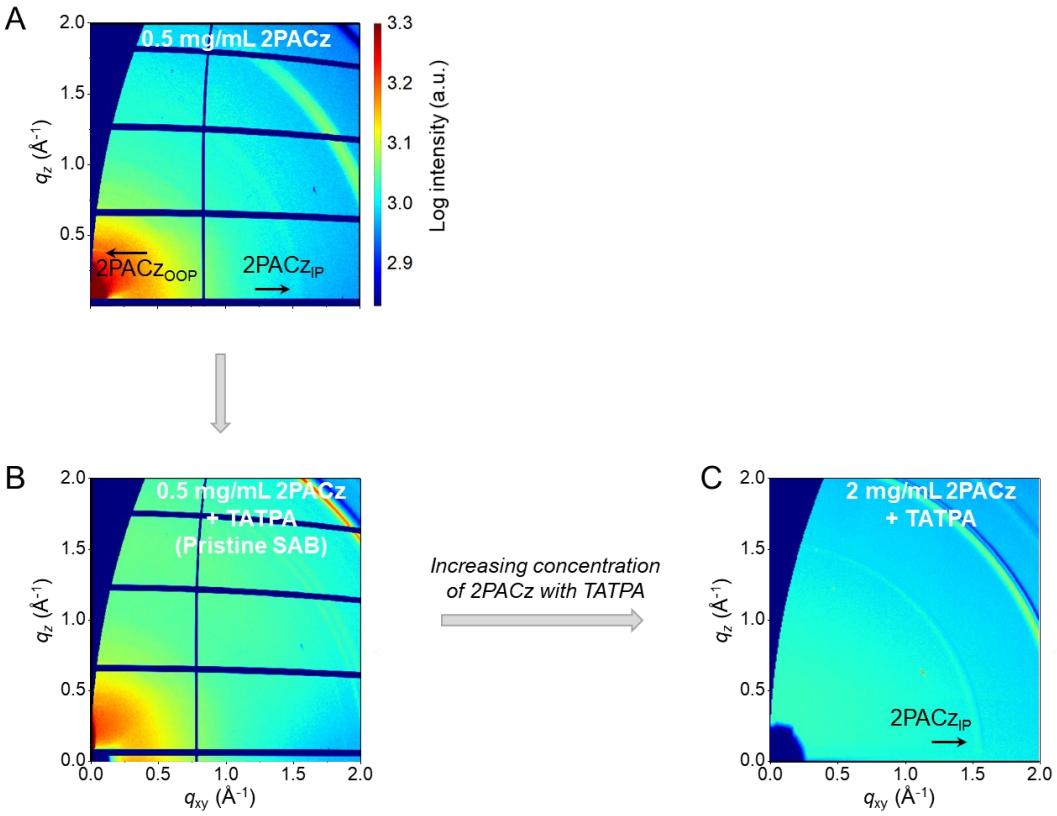

Supplementary Figure 26. GIWAXS results for SAM, SAB, and SAB with a concentrated 2PACz bottom layer. A. *Pristine SAM without the TATPA top layer.* ***B.*** *Original SAB described in the manuscript.* ***C.*** *The SAB featuring a higher concentration of the 2PACz precursor.*

We have provided GIWAXS spectra of SAB with a densely packed 2PACz monolayer, increasing the processing solution concentration from 0.5 mg mL^{-1} to 2 mg mL^{-1}. Prior GIWAXS analysis with a lower-concentrated solution showed that cross-coupling between TATPA and 2PACz disrupts the in-plane ordering of 2PACz assemblies, as evidenced by the disappearance of the scattering arc pattern at q_{xy} = 1.56 Å^{-1} (denoted as 2PACz$_{IP}$ in **Supplementary Figure 26B**). Increasing the density of 2PACz led to a reduction in molecular tilt for pristine SAMs. Upon introducing TATPA, the π-π stacking was again disrupted; however, instead of diminishing, the 2PACz$_{IP}$ appeared as an extended scattering arc in the GIWAXS spectra (**Supplementary Figure26C**), indicating a broader distribution of tilt angles compared to pristine SAMs. These

observations confirm that SAB formation triggers reorganization of the underlying 2PACz film assemblies.

Supplementary Note 5

Analysis of SAB structure

As shown in **Supplementary Figure 27**, the new peak at out-of-plane direction emerged at q_z = 1.75 $Å^{-1}$ clearly demonstrate the formation of preferred 'face-on' oriented TPA repeating unites, that is also illustrated in **Fig. 3j**. 3D presentation of the SAB is also shown in **Fig. 1f**.

We note that from our results of GIWAXS, 2PACz is not precisely 'edge-on' to the substrate, neither do the TPA moiety precisely 'face-on'. There is a preference for 2PACz to be 'edge-on' and triphenylamine moiety at SAB 'face-on'. Thus, the binding energies E_b at the p-*i* interface for the pristine 2PACz and SAB could vary slightly from the DFT predicted values.

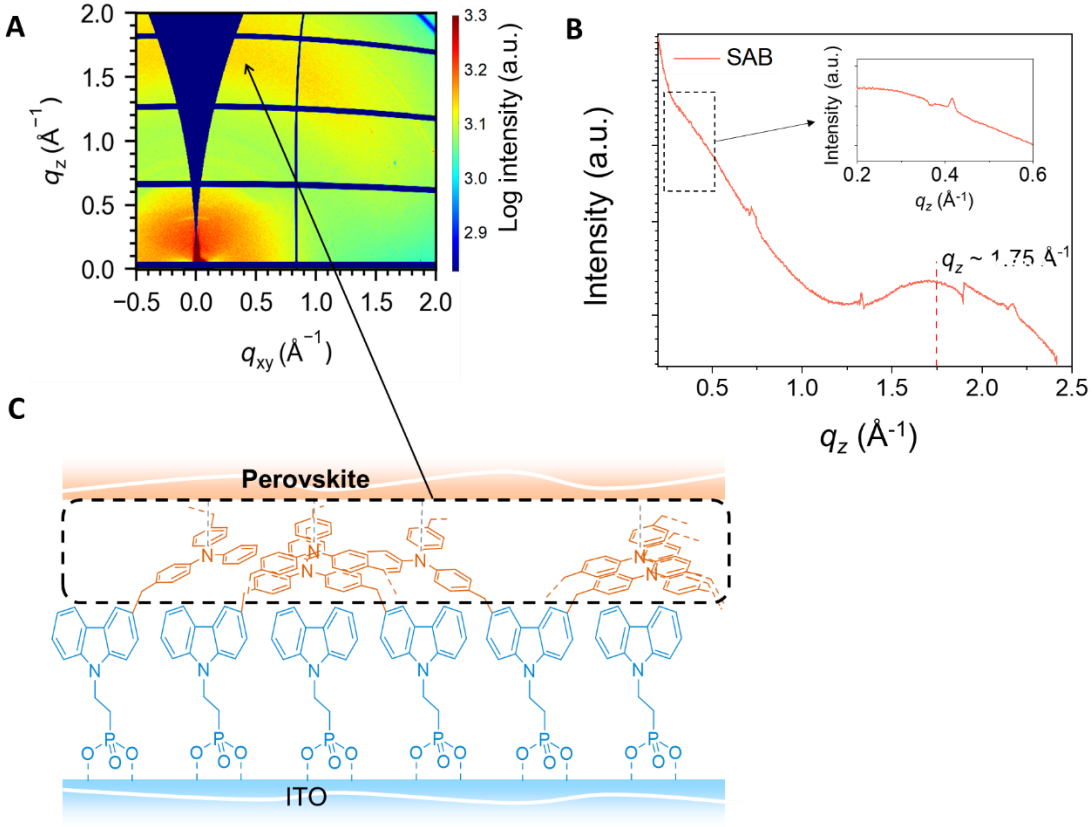

Supplementary Figure 27. Structural characterization of SAB. *A, 2D GIWAXS pattern and illustrative aggregation structure of SAB coated on ITO surface. The precursor concentration is adjusted to 0.5 mg/mL for 2PACz and 1 mg/mL for TATPA to observe the preferred orientation of the top triphenylamine (TPA) moiety of SAB.* ***B****, integration of the diffractions along out-of-plane direction, the inset indicates the out-of-plane aggregation peak of 2PACz.* ***C****, illustrative sketch showing the structure of SAB.*

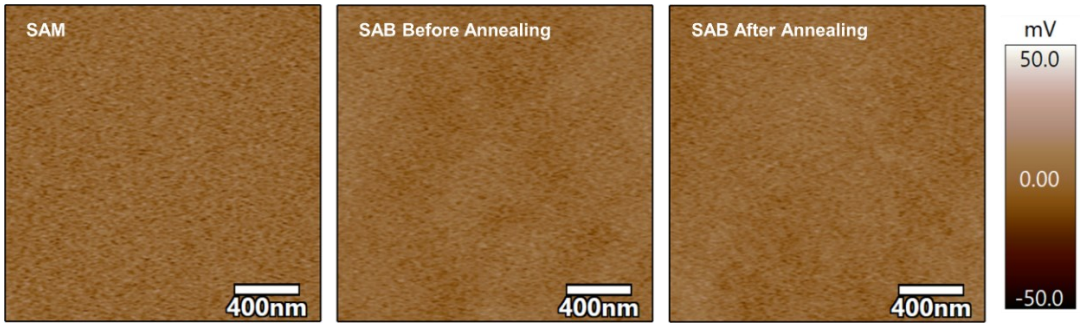

***Supplementary Figure 28**, KPFM surface potential images of SAM, SAB before annealing and SAB after annealing.*

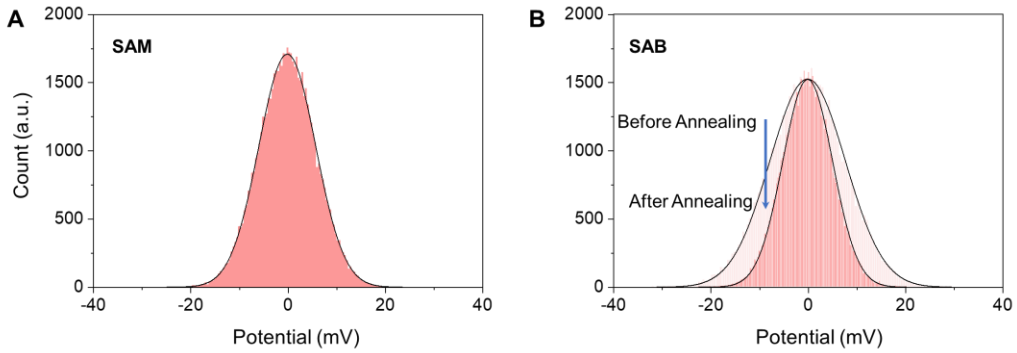

***Supplementary Figure 29**, **Contact potential difference (CPD) distribution of SAM, SAB before annealing and SAB after annealing.** The solid line shows the Gaussian distribution fit to the data.*

To monitor surface potential changes during the reaction between 2PACz and TATPA, we performed KPFM on 2PACz, unannealed 2PACz+TATPA, and annealed 2PACz+TATPA. The results, shown in **Supplementary Figures 28 and 29**, indicated that annealing led to a reduction in the contact potential difference (CPD) distribution of the SAB, with the full-width at half maximum (FWHM) decreasing from 18.3 mV to 12.1 mV. This suggests a more homogeneous surface due to the cross-linking between 2PACz and TATPA, which resulted in a more ordered structure. In contrast, no change in the FWHM was observed for the SAM after thermal annealing.

Supplementary Note 6

Analysis of area density after thermal cycle stress

We employed cyclic voltammetry (CV) to assess the areal densities of analytes adsorbed on TCO substrates. This technique quantifies the density of redox centers, which is indicative of the molecular coverage of electrochemically active species[17]. Given the similar oxidation potentials of the carbazole core in 2PACz and the triphenylamine moiety in the top layer[45,46], the total adsorbed molecules for SAB reflect their combined redox activities. This contrasts with the SAM sample, which only shows activity from 2PACz. Consequently, the higher initial values for SAB are attributed to the additional triphenylamine contributions (**Supplementary Figure 30**).

Elemental dispersive spectroscopy (EDS) analysis of fractured perovskite surfaces detected phosphorus elements (**Supplementary Figure 31**), indicating phosphonic acid molecules adhering to perovskites rather than TCO substrates. However, phosphorus signals were weak in EDS, with a higher ratio observed for perovskites deposited on SAM compared to those on SAB. We propose that the stronger covalent binding between SAB and TCO substrates could mitigate potential underestimations. This is supported by the lower molecular coverage loss on TCO substrates for SAB compared to SAM after thermal cycling, indicative of a robust interface resistant to desorption.

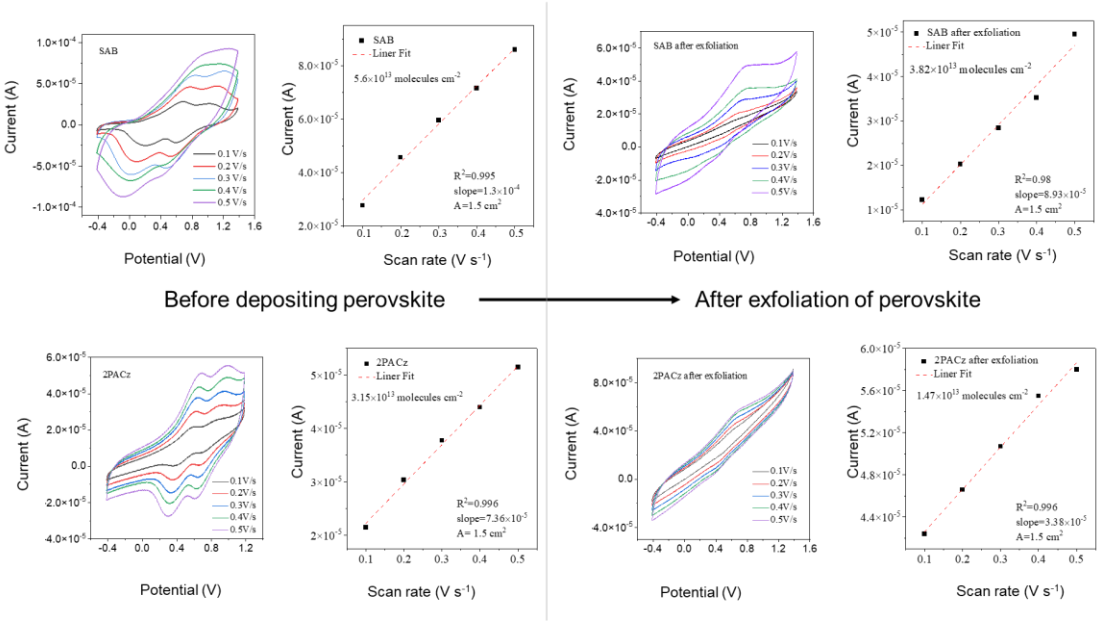

Supplementary Figure 30. electrochemical approach measured molecular coverage*, for freshly prepared 2PACz or SAB films, and exfoliated inverted PSCs after 1000 times thermal cycling tests between -40 °C and 85 °C, exposing 2PACz or SAB. A ferrocene redox couple external reference was applied calibrate the potential. The lines show the linear fit to the data.*

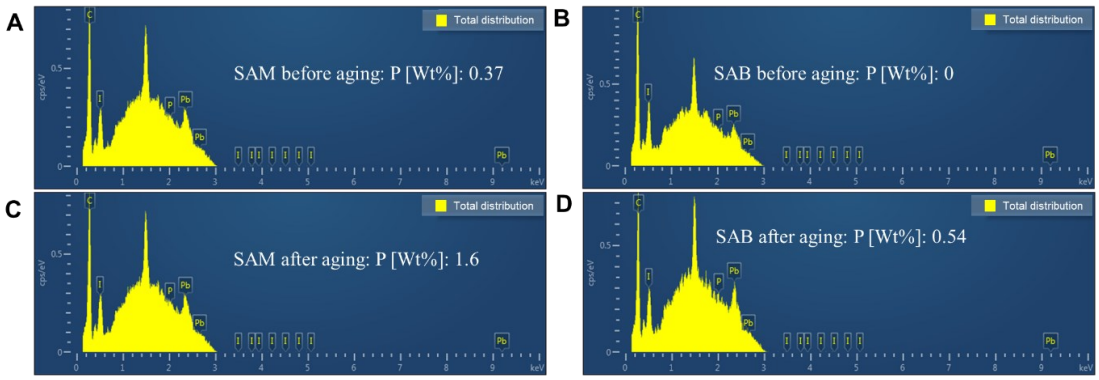

Supplementary Figure 31. EDS analysis showing the residues of SAM or SAB on the perovskite side of the buried interface*, indicated by the weight ratio of phosphorus.*

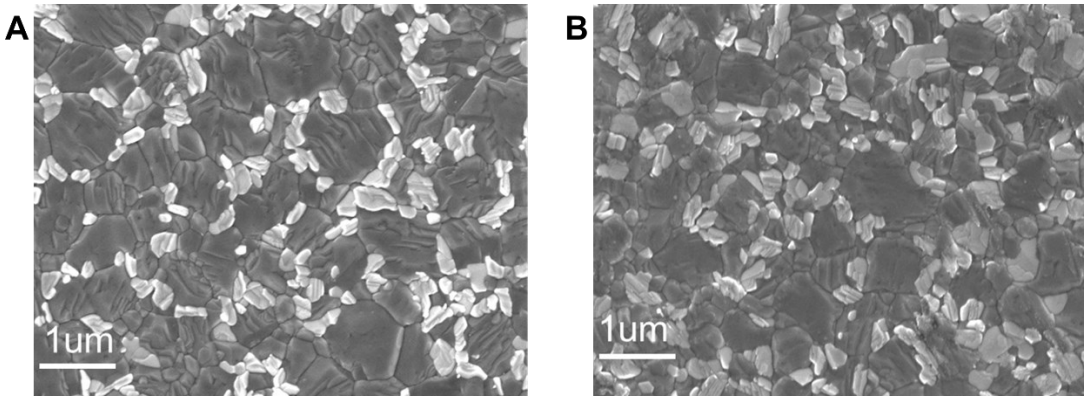

Supplementary Figure 32. Surface SEM photographs of perovskites, *deposited on 2PACz SAM* ***(a)*** *and SAB* ***(b)****.*

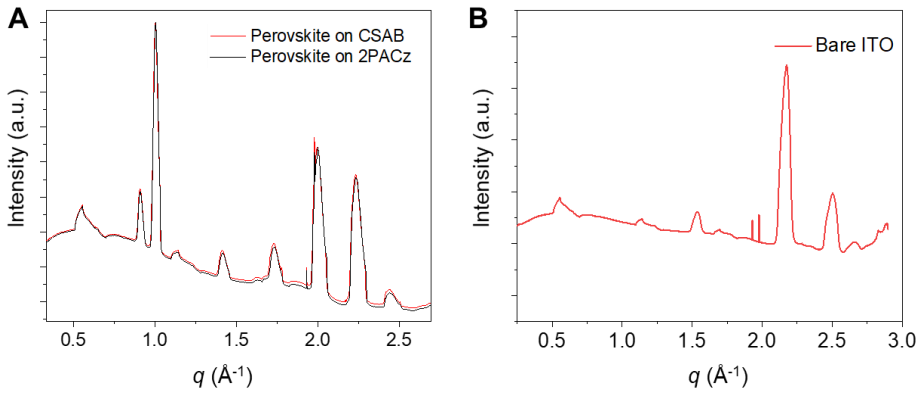

Supplementary Figure 33. GIWAXS integration of perovskite deposited on SAM and SAB *(A), with a bare ITO (B) as reference.*

The prominent peak observed between 0.5 and 0.75 $Å^{-1}$ is attributed to the Kapton tap adhered to the measurement container. During the GIWAXS measurement, the container was continuously purged with helium gas to enhance the signal-to-noise ratio for the molecularly thin SAM layer and to shield the film from ambient moisture. GIWAXS measurements of a bare ITO film within the container also showed the same scattering peak in the range of 0.5 and 0.75 $Å^{-1}$ (**Supplementary Figure 33B**).

Supplementary Note 7

TRPL and PLQY characterization to SAB on perovskite

We have measured PL lifetimes at different fluences and several spots of the sample.[71] Notably, the decay time varies with PL flux in a manner that adheres to a power-law relationship. We have therefore conducted PL decay measurements across excitation fluxes ranging from 12 nJ cm^{-2} to 718 nJ cm^{-2} (**Supplementary Figure 34A** and **34B**). Independent measurements were performed at multiple locations on each substrate to ensure data representation. We found that perovskite/SAB films consistently show longer PL decay across all excitation intensities compared to perovskite/SAM films, albeit with variations in decay times at different spots (**Supplementary Figure 34C** and **34D**). These results support the main finding from steady-state PL measurements that defect trapping is reduced at the perovskite/SAB interface.

Non-radiative recombination was assessed using photoluminescence quantum yield (PLQY) measurements (**Supplementary Figure 35**), which directly relate to device V_{oc}. The perovskite film on SAB exhibited a PLQY of 13.2%, compared to 6.9% on SAM, indicating reduced non-radiative recombination – likely due to improved passivation at the buried interface. We calculated the quasi-Fermi-level splitting (QFLS) of perovskite films and compared it with the qV_{oc} of the corresponding devices, where q stands for elementary charge.[72,73] The perovskite film on SAB showed a QFLS increase of approximately 13 meV compared to SAM, accounting for the relatively small V_{oc} differences between PSCs based on SAM and SAB. Nevertheless, the gap between qV_{oc} and QFLS are reduced for SAB devices, indicating better energetic alignment at the interfaces – consistent with UPS measurements.[70]

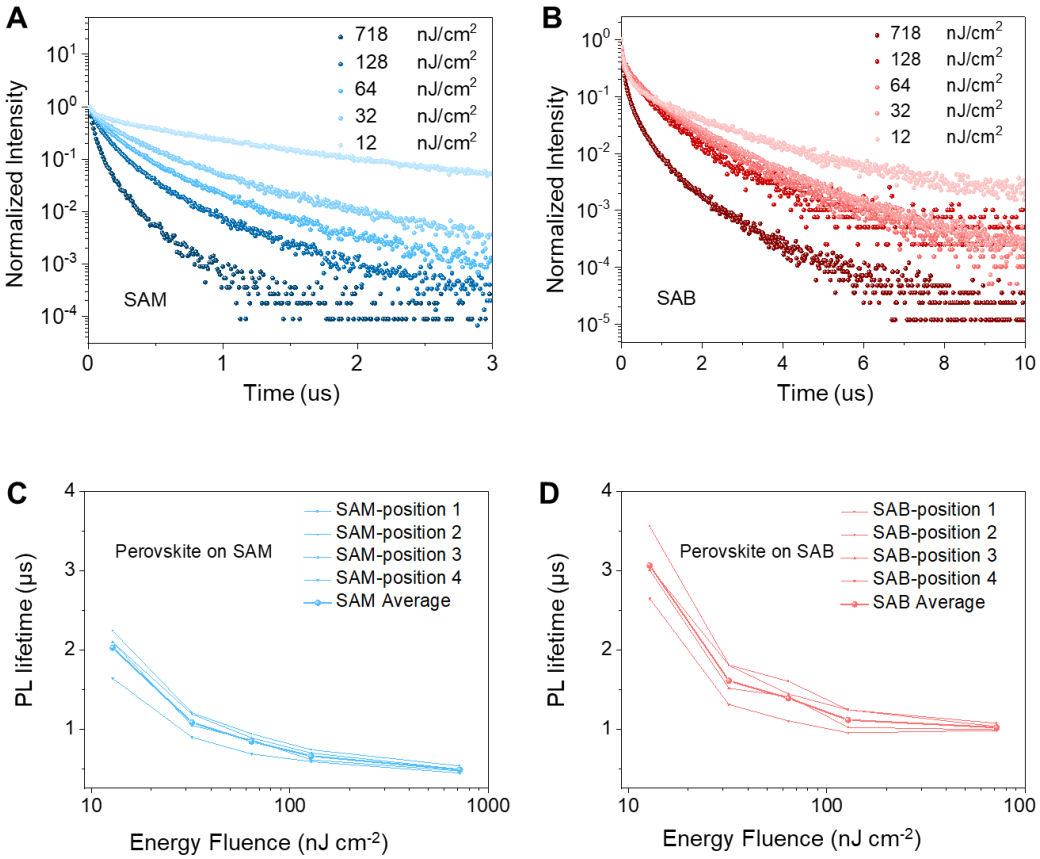

Supplementary Figure 34. Time-Resolved Photoluminescence (TRPL) characterization results of perovskite on SAM and SAB. ***A, B****, TRPL decay profiles of perovskite films deposited on SAM and SAB hole-selective contacts.* ***C, D****, Summary of TRPL decay times for perovskite films deposited on SAM or SAB, with measurements conducted at four different positions on each sample.*

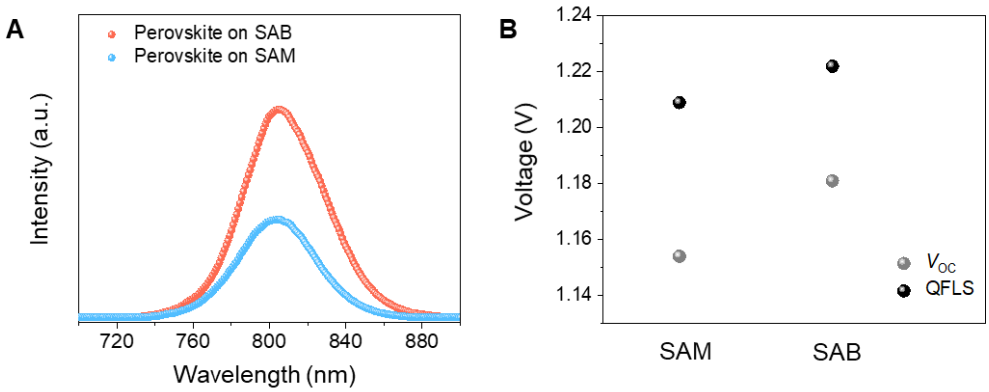

Supplementary Figure 35. Photoluminescence characterization results of perovskite on SAM and SAB. A, *Photoluminescence spectra of perovskite films deposited on SAM and SAB.* ***B,*** *comparison of* V_{oc} *and QFLS for PSC devices based on SAM and SAB.*

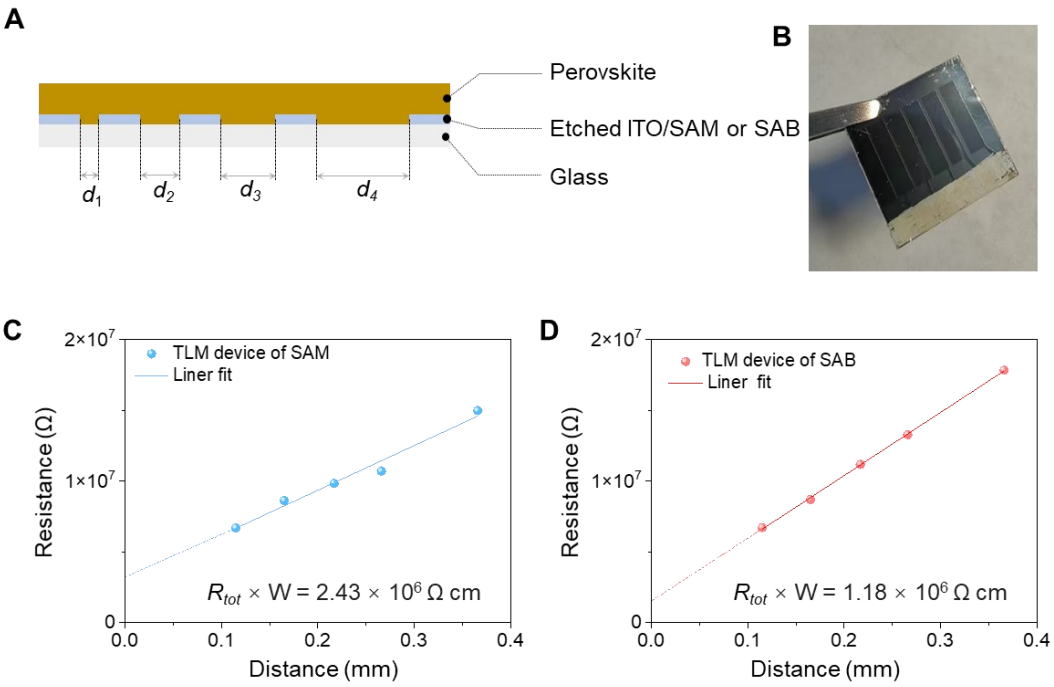

Supplementary Figure 36. transmission line model (TLM) measurement on contact resistance of perovskite on SAM and SAB. ***A*** *and* ***B****, Schematic diagram and an image of device setup for the TLM analysis.* ***C*** *and* ***D****, Contact resistance (R_c) results as calculated by the TLM. R_c equals to the extrapolated total resistance (R_{tot}) at a distance of 0 mm times the line width (W). The lines show the linear fit to the data.*

we employed the transmission line method (TLM) to calculate the contact resistivity (R_C)[47]. The test structure utilized laser-patterned ITO substrates with variable spacing between contacts (**Supplementary Figure 36**). Conductivity measurements between electrode pairs at know distances revealed that the R_C at the perovskite/SAB interface is reduced by over 50% compared to the interface with 2PACz SAM. This reduction supports the intimate interface contact between perovskites and SAB, as predicted by DFT calculations.

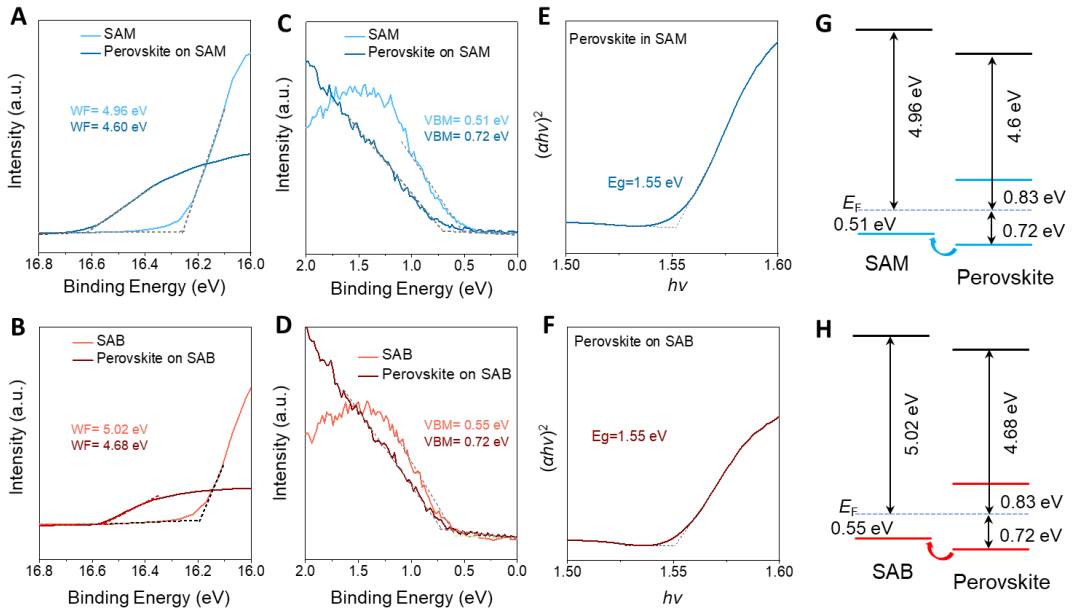

Supplementary Figure 37, UPS characterization results of SAM and SAB. A-D*, UPS results of SAM, SAB, perovskite on SAM, and perovskite on SAB.* ***E*** *and* ***F****, optical bandgaps of perovskites on SAM and SAB.* ***G*** *and* ***H****, Band alignment diagram of the perovskite/SAM stack and perovskite/SAB stack. WF: work function; VBM: valance band maxima, Eg: Bandgap. The dashed lines represent the extrapolations used to determine the onset position.*

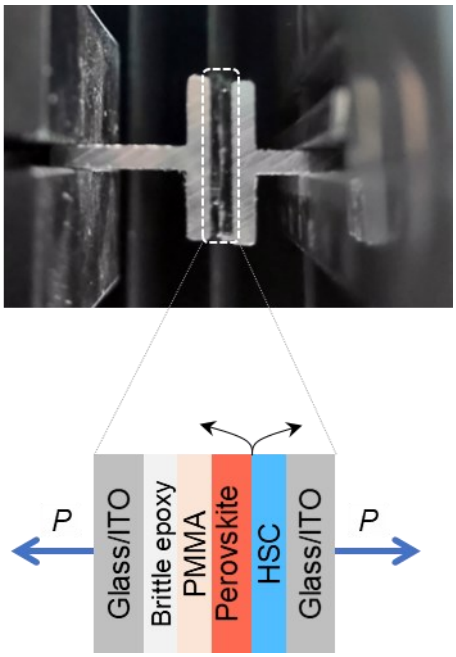

Supplementary Figure 38. *a photograph and* ***illustrative sketch of the double-cantilever beam (DCB) fabricated to measure the interface toughness*** G_C. *HSC represents hole-selective contact; P represents the load force.*

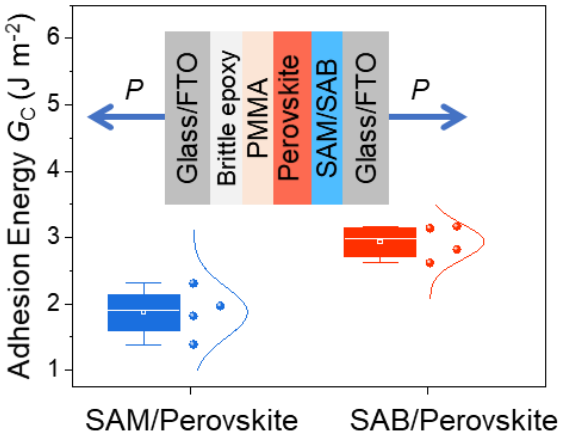

Supplementary Figure 39, Adhesion energy statistic distribution of the perovskite/HSC contact using and FTO as substrate. *The central lines in the box represent the medians, upper and lower limit of the box are quartiles, hallowed data points are averages and the upper and lower bars are 1.5x interquartile range, among 4 measurements. The solid line shows the Gaussian distribution fit to the data. P represents the load force.*

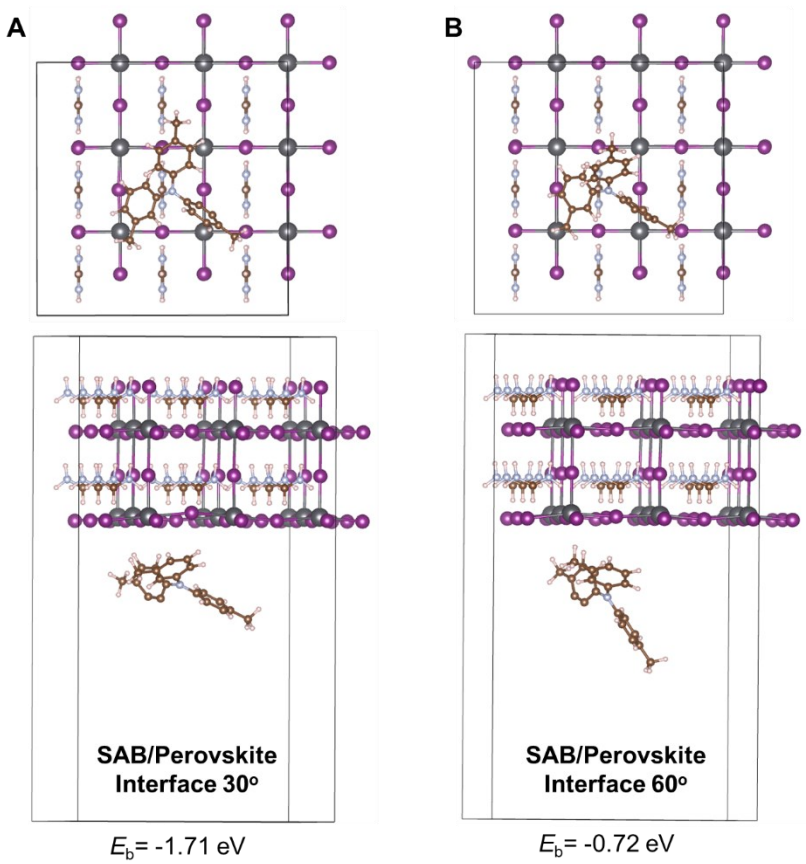

Supplementary Figure 40. Calculated adsorption energy between SAB and perovskite with different dihedral angle*. The dihedral angle between triphenylamine moiety on SAB and perovskite lattice set to 30° (A) and 60° (B).*

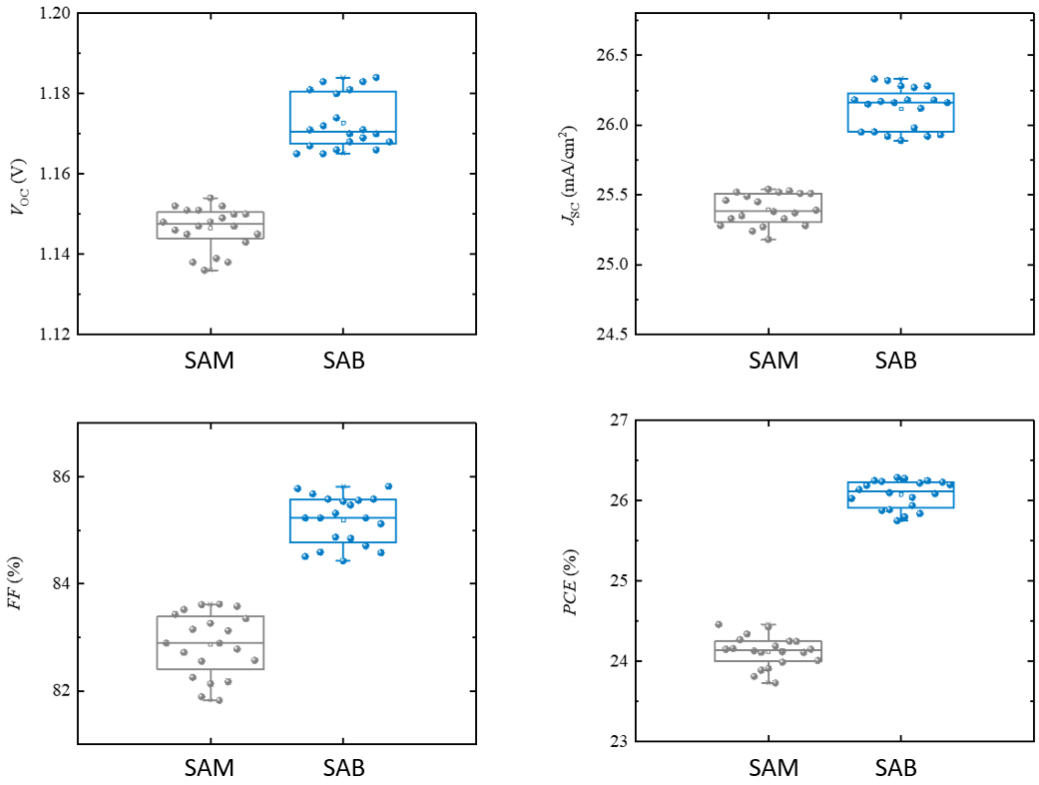

Supplementary Figure 41. statistic results for inverted PSCs with pristine 2PACz SAM and SAB hole-selective contact. *The central lines in the box represent the medians, upper and lower limit of the box are quartiles, hallowed data points are averages and the upper and lower bars are 1.5x interquartile range, among 20 devices.*

Supplementary Table 1, Device parameter statistics of 20 individual PSCs based on pristine 2PACz SAM.

2PACZ	Voc (V)	Jsc(mA/cm^2)	FF(%)	PCE(%)
1	1.154	25.54	82.89	24.43
2	1.151	25.38	82.55	24.11
3	1.152	25.27	82.13	23.91
4	1.148	25.45	82.78	24.19
5	1.139	25.33	83.62	24.13
6	1.151	25.24	82.25	23.89
7	1.150	25.52	82.17	24.12
8	1.147	25.49	83.26	24.34
9	1.152	25.18	81.82	23.73
10	1.136	25.53	83.61	24.25
11	1.138	25.52	83.58	24.27
12	1.149	25.37	83.15	24.25
13	1.145	25.51	82.72	24.16
14	1.147	25.46	82.57	24.11
15	1.146	25.35	83.12	24.15
16	1.150	25.28	81.89	23.81
17	1.143	25.33	83.43	24.15
18	1.148	25.51	83.52	24.46
19	1.138	25.39	83.35	24.01
20	1.145	25.28	82.89	23.99

Supplementary Table 2. Device parameter statistics of 20 individual PSCs based on SAB.

Polymer-2PACZ	Voc (V)	Jsc(mA/cm^2)	FF(%)	PCE(%)
1	1.170	26.28	85.47	26.28
2	1.168	25.89	85.32	25.80
3	1.174	26.18	85.54	26.29
4	1.171	25.92	84.85	25.75
5	1.181	25.98	84.87	26.04
6	1.166	26.16	85.58	26.10
7	1.169	26.32	85.23	26.22
8	1.180	25.95	84.71	25.94
9	1.183	26.27	84.43	26.24
10	1.165	26.33	85.56	26.25
11	1.172	25.92	85.23	25.89
12	1.166	26.28	85.68	26.25
13	1.170	25.95	85.12	25.84
14	1.167	26.12	85.58	26.09
15	1.183	26.17	84.59	26.19
16	1.168	26.18	85.78	26.23
17	1.165	26.15	85.82	26.14
18	1.171	25.93	85.23	25.88
19	1.184	26.16	84.58	26.20
20	1.181	26.08	84.51	26.03

Supplementary Figure 42. independent measurement results from Shanghai Institute of Microsystem and information Technology, Chinese Academy of Sciences (SIMIT).

Report No. 23TR102509

Sample Information

Sample Type	Perovskite solar cell
Serial No.	9-1-1#
Lab Internal No.	23102501-9#
Measurement Item	I-V characteristic
Measurement Environment	23.9±2.0°C,41.3±5.0%R.H

Measurement of I-V characteristic

Reference cell	PVM 1121
Reference cell Type	mono-Si, WPVS, calibrated by NREL (Certificate No. ISO 2075)
Calibration Value/Date of Calibration for Reference cell	144.53mA/ Feb. 2023
Measurement Conditions	Standard Test Condition (STC): Spectral Distribution: AM1.5 according to IEC 60904-3 Ed.3, Irradiance: 1000±50W/m², Temperature: 25±2°C
Measurement Equipment/ Date of Calibration	AAA Steady State Solar Simulator (YSS-T155-2M) / July.2023 IV test system (ADCMT 6246) / June. 2023 Measuring Microscope (MF-B2017C) / July.2023 SR Measurement system (CEP-25ML-CAS) / April.2023
Measurement Method	I-V Measurement: Logarithmic sweep in both directions (Voc to Isc and Isc to Voc) during one flash based on IEC 60904-1:2020. Spectral Mismatch factor was calculated according to IEC 60904-7 and I-V correction according to IEC 60891.
Measurement Uncertainty	Area: 1.0%(k=2); Isc: 1.9%(k=2); Voc: 1.0%(k=2); Pmax: 2.4%(k=2); Eff: 2.5%(k=2)

2 / 4

====Measurement Results ====

	Forward Scan (Isc to Voc)	Reverse Scan (Voc to Isc)
Area	10.01 mm^2	
Isc	2.630 mA	2.628 mA
Voc	1.185 V	1.185 V
Pmax	2.606 mW	2.611 mW
Ipm	2.526 mA	2.550 mA
Vpm	1.032 V	1.024 V
FF	83.65 %	83.84 %
Eff	26.04 %	26.08 %

- Spectral Mismatch Factor: SMM=0.9950.
- Designated illumination area defined by a thin mask was measured by measuring microscope.
- Test results listed in this measurement report refer exclusively to the mentioned measured sample.
- The results apply only at the time of the test, and do not imply future performance.

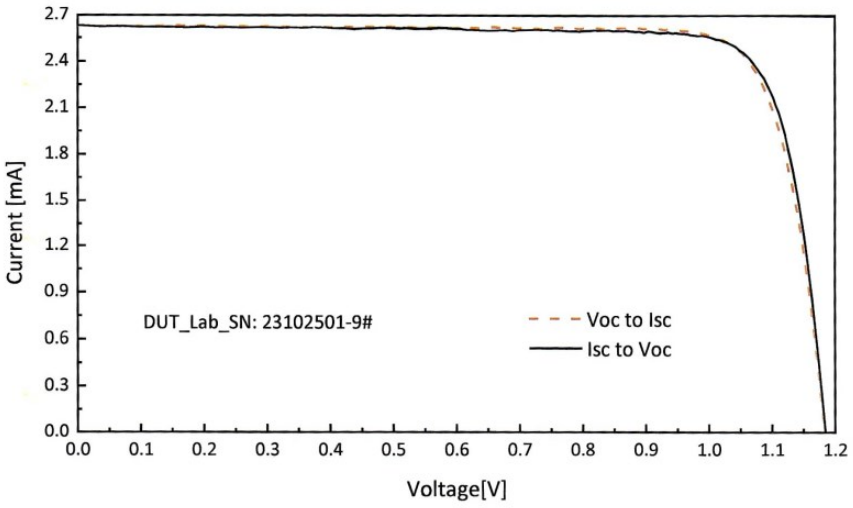

Fig.1 I-V curves of the measured sample

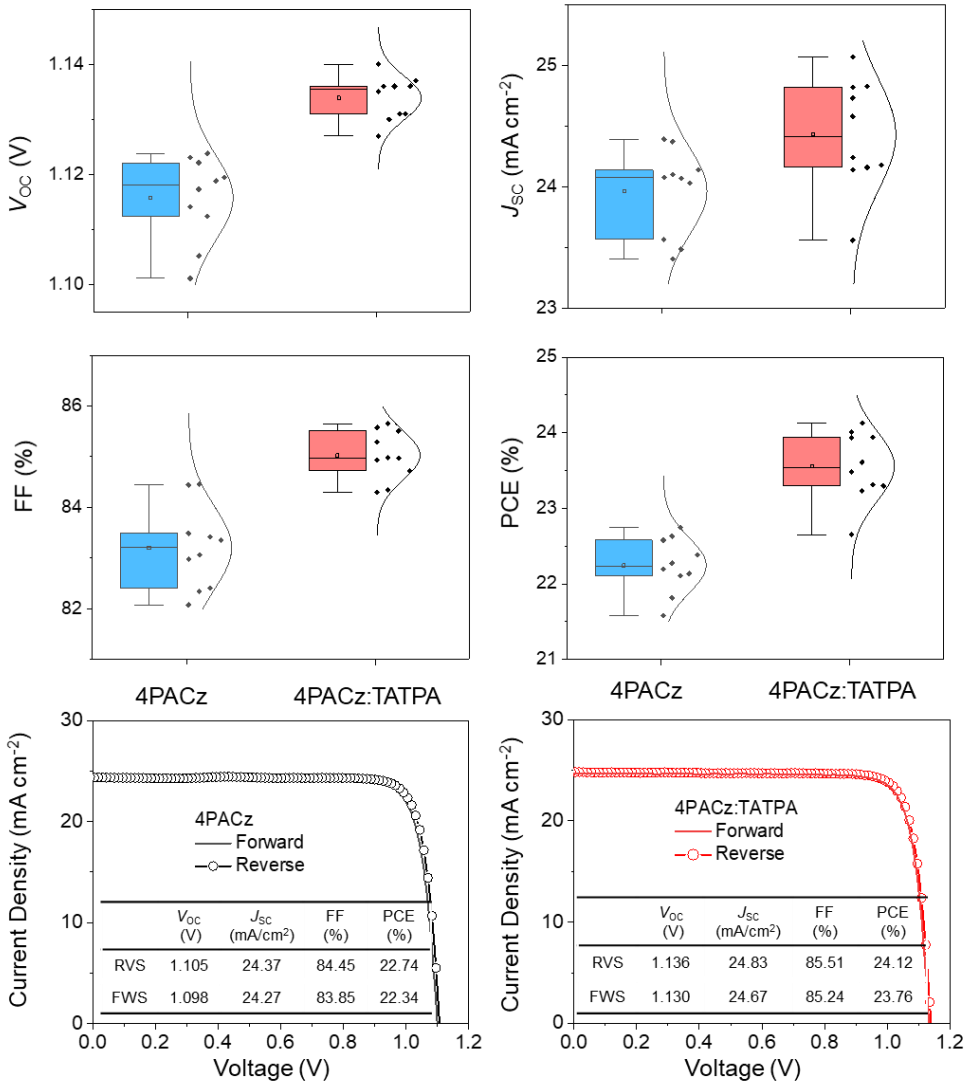

Supplementary Figure 43. Photovoltaic parameter statistical distribution of PSCs using 4PACz and 4PACz:TATPA (4PACz-SAB) as hole-selective contacts. *The central lines in the box represent the medians, hallowed data points are averages, upper and lower limit of the box are quartiles and the upper and lower bars are 1.5x interquartile range, among 10 devices. The solid line shows the Gaussian distribution fit to the data. The structures of 4PACz and 4PACz-SAB can be seen in* ***Supplementary Figure 20****; The forward and reverse scan IV curves for the champion PSCs based on 4PACz and 4PACz-SAB are also provided, in which SAB devices exhibited smaller hysteresis compared to their SAM-based counterparts. The scan step is 20 mV with a delay time of 50 ms per step.*

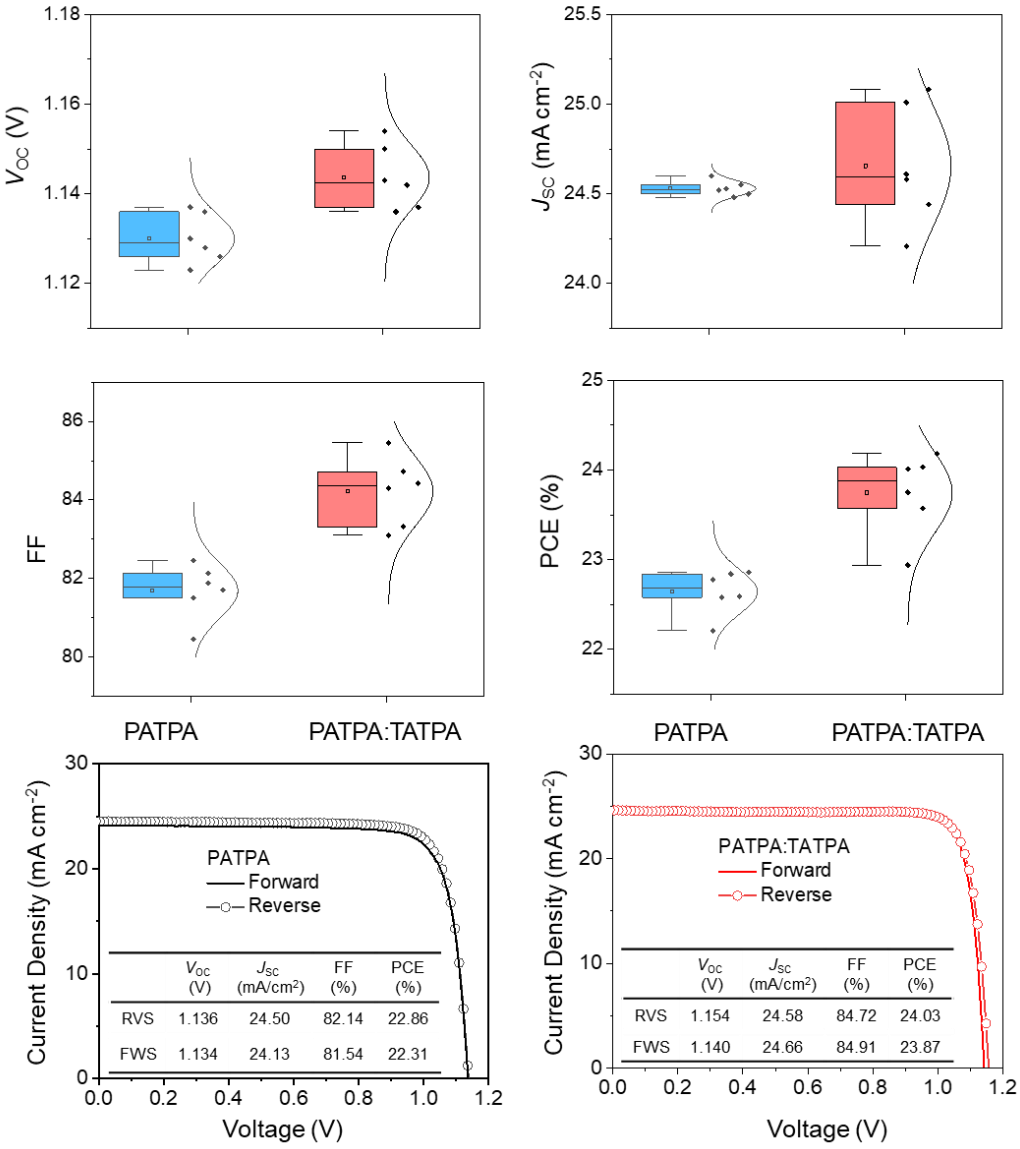

Supplementary Figure 44. Photovoltaic parameters statistical distribution of PSCs using PATPA and PATPA:TATPA (PATPA-SAB) as hole-selective contacts. *The central lines in the box represent the medians, hallowed data points are averages, upper and lower limit of the box are quartiles and the upper and lower bars are 1.5x interquartile range, among 6 devices. The solid line shows the Gaussian distribution fit to the data. The structures of PATPA and PATPA-SAB can be seen in* ***Supplementary Figure 20****. The forward and reverse scan IV curves for the champion PSCs based on PATPA and PATPA-SAB are also provided, in which SAB devices exhibited smaller hysteresis compared to their SAM-based counterparts. The scan step is 20 mV with a delay time of 50 ms per step.*

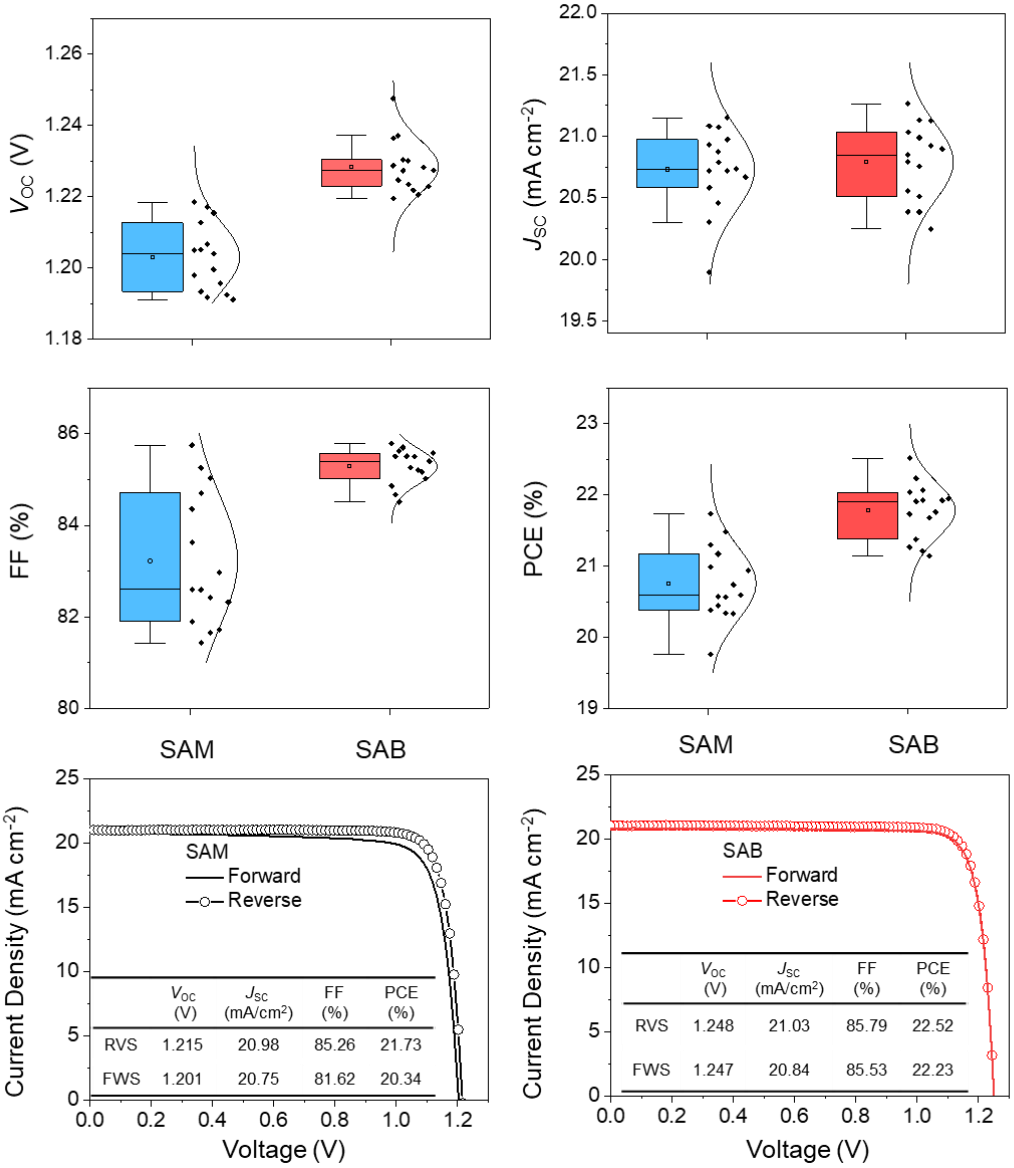

Supplementary Figure 45. Photovoltaic parameters statistical distribution of 1.68-eV PSCs ($Cs_{0.21}FA_{0.74}MA_{0.05}Pb(I_{0.81}Br_{0.14}Cl_{0.05})_3$) utilizing SAM or SAB as the hole-selective contact. *The central lines in the box represent the medians, hallowed data points are averages, upper and lower limit of the box are quartiles and the upper and lower bars are 1.5x interquartile range, among 15 devices. The solid line shows the Gaussian distribution fit to the data. The forward and reverse scan IV curves for the champion 1.68 eV PSCs based on SAM and SAB are also provided, in which SAB devices exhibited smaller hysteresis compared to their SAM-based counterparts. The scan step is 20 mV with a delay time of 50 ms per step.*

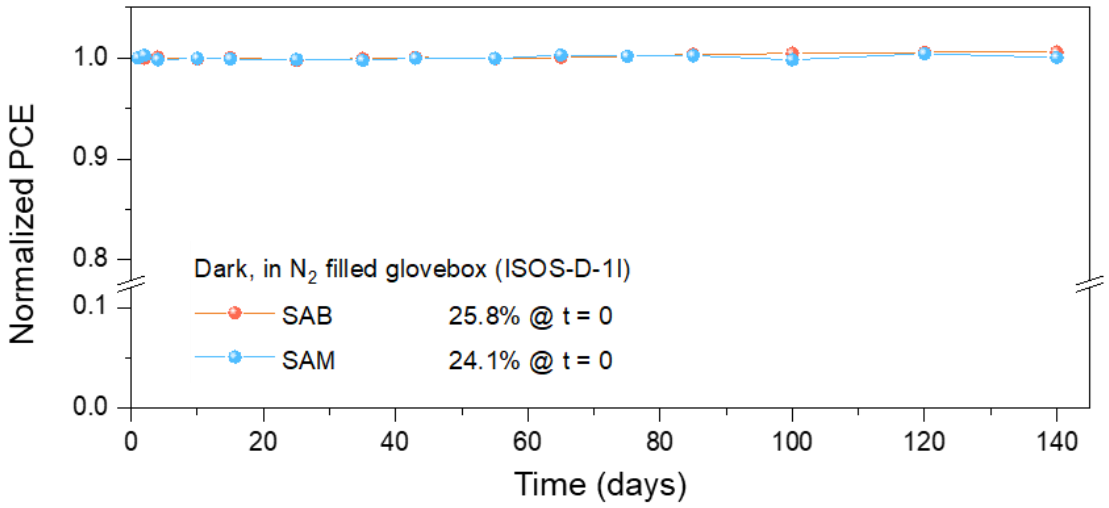

Supplementary Figure 46. device performance decay for 140 days stored in dark under N_2 protection at room temperature.

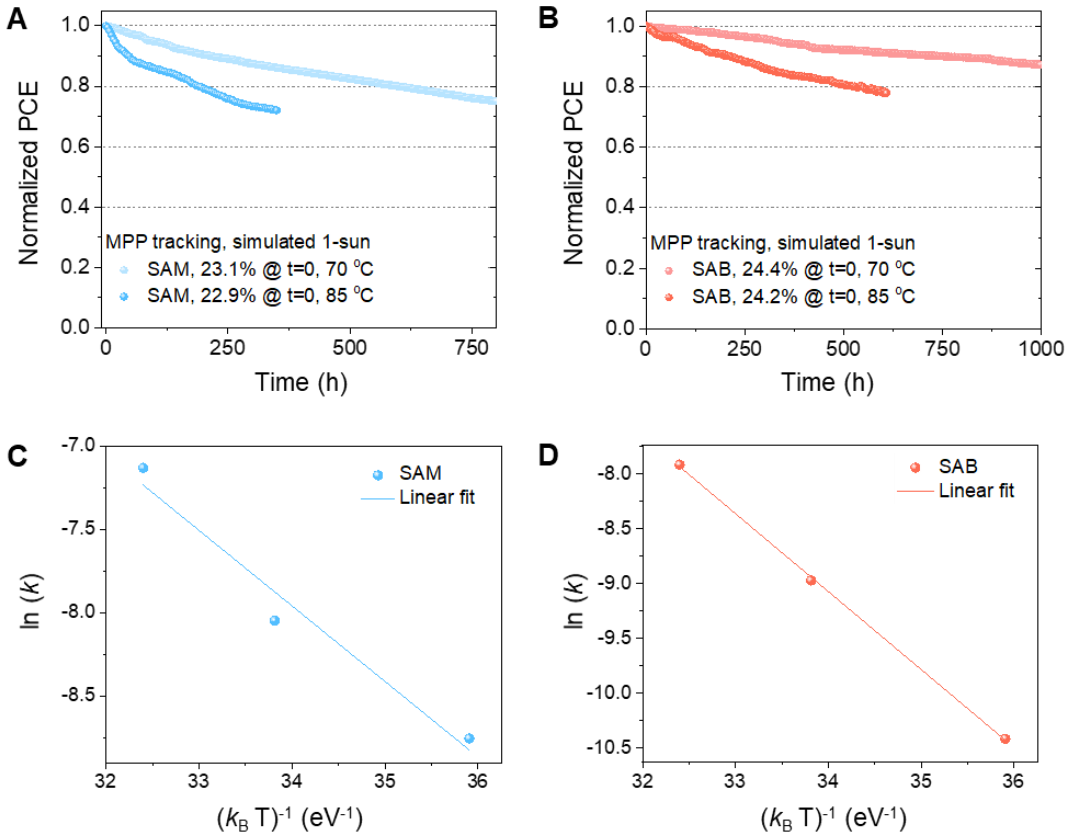

Supplementary Figure 47, MPPT Stability results of PSCs based on SAM and SAB. The cells are under simulated 1-sun illumination and held at 70 °C and 85 °C.

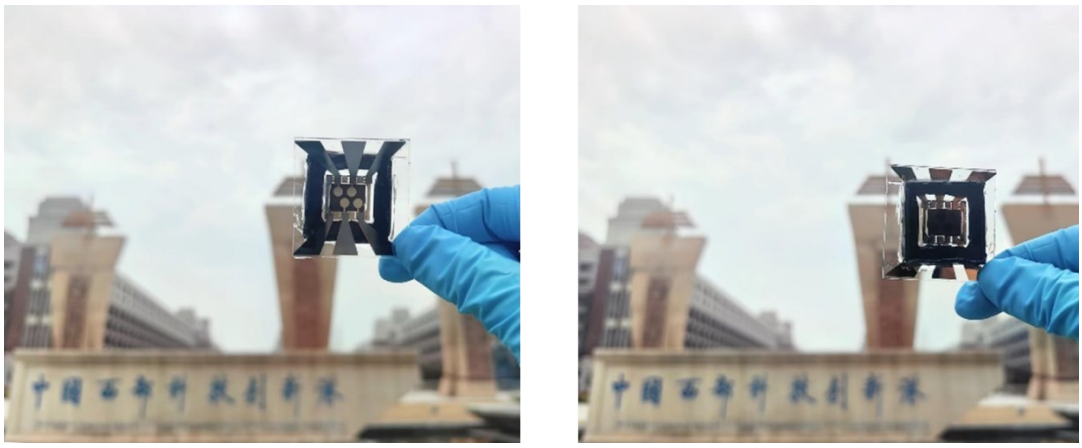

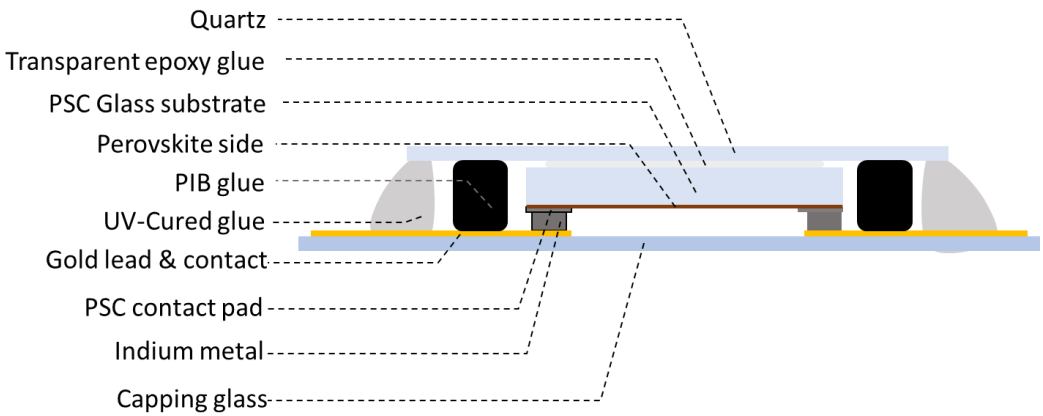

Supplementary Figure 48. Photographs and a cross-section sketch showing our device that has been double-encapsulated by PIB and UV-cured glue. *The leads outside are used to create contact to measure device performance. A thin layer of transparent epoxy glue was applied between the quartz and the device to avoid additional reflective loss due to the introduction of the air gap.*

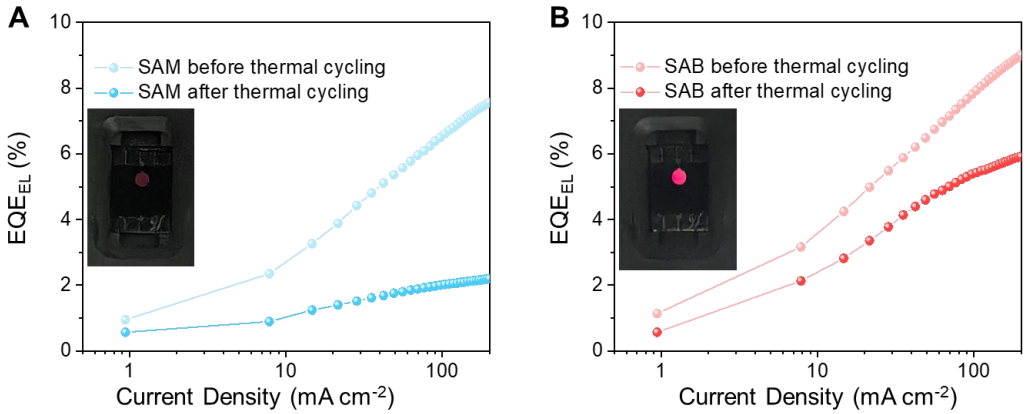

Supplementary Figure 49. A, B, EQE_{EL} results for aged PSCs using SAM and SAB as hole-selective contacts after thermal cycling. *Inset: Images of the devices emitting electroluminescence measured at a current density of 28 mA* cm^{-2}.

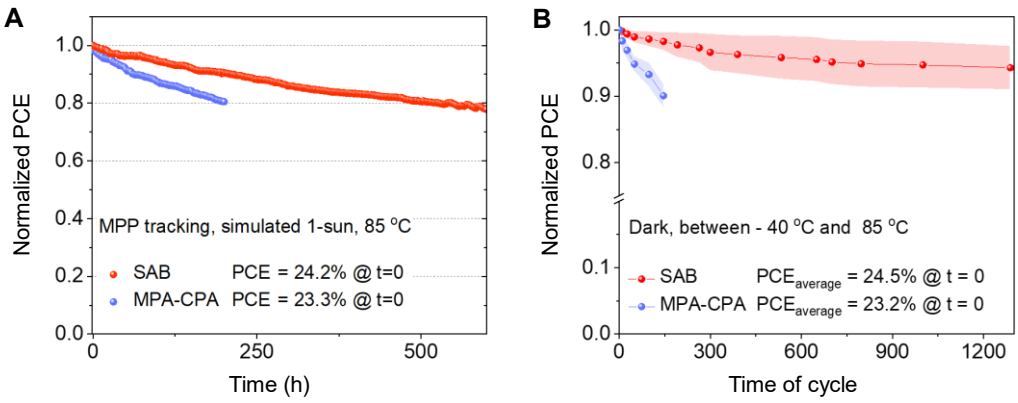

Supplementary Figure 50. Stability of PSCs based on MPA-CPA and SAB, *during MPPT (**A**) and thermal cycling (**B**). Data in (**B**) are presented as mean values +/- standard derivations (SD). Error bands in (**B**): for SAB is SD of data among 7 devices; for MPA-CPA is SD of data among 3 devices.*

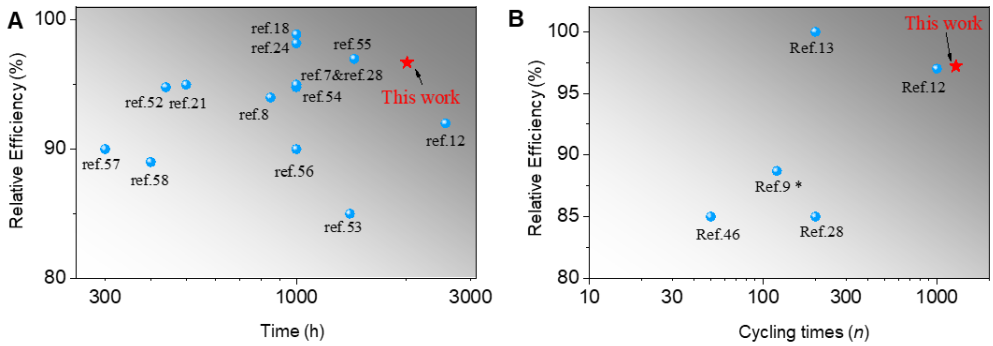

Supplementary Figure 51. recent reports on damp heat (A) and thermal cycling (B) stabilities based on IEC61215:2016 protocols. *(Ref.9* thermal cycles tested between −60° and 80°C).*

Supplementary Table 3. Summary of stability data for PSCs under damp-heat conditions (85°C and 85% relative humidity). *"N/A" indicates that the initial PCE value before measurement was not reported.*

Initial PCE	***Testing hours***	***PCE retained (%)***	***Degradation rate (rel. % h^{-1})***	***Reference***
N/A	*2560*	*92*	*0.0031*	*Nature 623, 313-318 (2023).*[12]
N/A	*1000*	*95*	*0.0050*	*Science 376, 416-420 (2022).*[28]
N/A	*850*	*94*	*0.0071*	*Nature 611, 278-283 (2022).*[8]
N/A	*1400*	*85*	*0.0107*	*Energy & Environmental Materials 6, e12434 (2023).*[53]
N/A	*440*	*94.8*	*0.0118*	*Advanced Materials 35, 2211155 (2023) .*[52]
N/A	*1000*	*98.9*	*0.0011*	*Science 383, 1236-1240 (2024).*[18]
N/A	*1000*	*94.8*	*0.0052*	*Advanced Materials Technologies 4, 1800390 (2019).*[54]
20.50%	*1200*	*95*	*0.0041*	*Science 376, 73-77 (2022).*[7]
25.30%	*400*	*89*	*0.0275*	*Science 383, 524-531 (2024).*[58]
24.80%	*1000*	*98.2*	*0.0018*	*Nature Energy 8, 839-849 (2023).*[24]
24.32%	*1000*	*90*	*0.0100*	*Nature Energy 8, 946-955 (2023).*[56]
23.30%	*1440*	*97*	*0.0021*	*Nature Energy 7, 520-527 (2022).*[55]
23%	*500*	*95*	*0.0100*	*Science 380, 404-409 (2023).*[21]
21.80%	*300*	*90*	*0.0333*	*Nature 624, 557-563 (2023).*[57]
24.20%	***2000***	***96.7***	***0.0017***	***This work***

Supplementary Table 4. Summary of stability data for PSCs under thermal cycling from -40°C to 85°C. *"N/A" indicates that the initial PCE value before measurement was not reported.*

Initial PCE	***Testing cycles***	***PCE retained (%)***	***Degradation rate (rel. % h^{-1})***	***Reference***
N/A	*50*	*85*	*0.3000*	*Energy & Environmental Materials 6, e12434 (2023).*[53]
N/A	*200*	*85*	*0.0750*	*Science 376, 416-420 (2022).*[28]
N/A	*1000*	*97*	*0.0030*	*Nature 623, 313-318 (2023).*[12]
N/A	*120*	*88.7*	*0.0942*	*Science 379, 399-403 (2023).*[9]
N/A	*200*	*100*	*0.0000*	*Joule 4, 2646-2660 (2020).*[13]
24.50%	***1200***	***97.2***	***0.0023***	***This work***

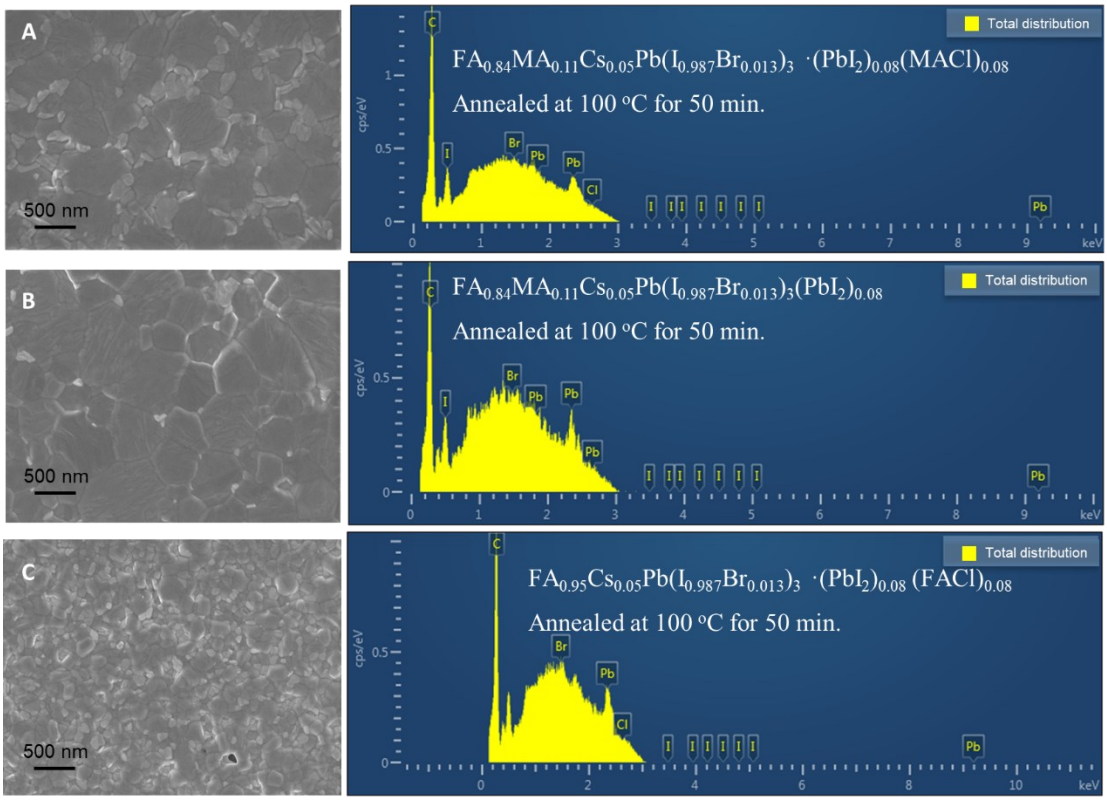

Supplementary Figure 52, Surface SEM images and EDS spectra of the perovskite films upon annealing at 100 °C for 50 min.

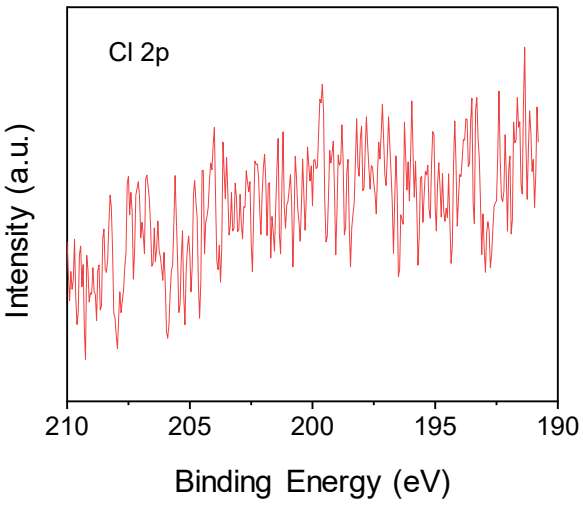

Supplementary Figure 53, XPS spectrum of the perovskite film containing 8% MACl in its precursor, and annealed at 100 °C for 50 min.

Supplementary References

68 Lockyer, N. P. *et al.* Secondary ion mass spectrometry. *Nature Reviews Methods Primers* **4,** 32*,* (2024).

69 Ren, Z. *et al.* Poly(carbazole phosphonic acid) as a versatile hole-transporting material for p-i-n perovskite solar cells and modules. *Joule* **7**, 2894-2904, (2023).

70 Ah, C. S. *et al.* Optical and Electrical Properties of Electrochromic Devices Depending on Electrolyte Concentrations and Cell Gaps. *Bull. Korean Chem. Soc.* **37**, 1812-1819, (2016).

71 Yuan, Y. *et al.* Shallow defects and variable photoluminescence decay times up to 280 μs in triple-cation perovskites. *Nat. Mater.* **23**, 391-397, (2024).

72 Caprioglio, P. *et al.* On the Relation between the Open-Circuit Voltage and Quasi-Fermi Level Splitting in Efficient Perovskite Solar Cells. *Adv. Energy Mater.* **9**, 1901631, (2019).

73 Zhu, H. *et al.* Tailored Amphiphilic Molecular Mitigators for Stable Perovskite Solar Cells with 23.5% Efficiency. *Adv. Mater.* **32**, 1907757, (2020).